INTERACTION OF keV PHOTONS WITH MATTER AND NEW APPLICATIONS

R. CESAREO

Centro per l'Ingegneria Biomedica e Dipartimento di Energetica,
Università di Roma "La Sapienza", Rome, Italy

A.L. HANSON

Brookhaven National Laboratory, Upton, New York 11973, USA

G.E. GIGANTE

Centro per l'Ingegneria Biomedica e Dipartimento di Fisica,
Università di Roma "La Sapienza", Rome, Italy

L.J. PEDRAZA

International Atomic Energy Agency, Vienna, Austria

S.Q.G. MAHTABOALLY

Department of Physics, University of Rajshahi, Rajshahi, Bangladesh

NORTH-HOLLAND

INTERACTION OF keV PHOTONS WITH MATTER AND NEW APPLICATIONS

R. CESAREO

Centro per l'Ingegneria Biomedica e Dipartimento di Energetica, Università di Roma "La Sapienza", Rome, Italy

A.L. HANSON

Brookhaven National Laboratory, Upton, New York 11973, USA

G.E. GIGANTE

Centro per l'Ingegneria Biomedica e Dipartimento di Fisica, Università di Roma "La Sapienza", Rome, Italy

L.J. PEDRAZA*

International Atomic Energy Agency, Vienna, Austria

S.Q.G. MAHTABOALLY

Department of Physics, University of Rajshahi, Rajshahi, Bangladesh

Contents:

The fundamental interactions of keV photons with matter, i.e. photoelectric effect and coherent and incoherent scattering are treated from a non-traditional point of view. Section 1 is designed to lay a foundation of the basic science. Section 2 deals with non-imaging analytical techniques that have been developed over the past 20 or so years. These techniques include energy-dispersive X-ray fluorescence, Compton profile measurements, and general scattering techniques. In section 3, imaging techniques are described. These imaging techniques utilize the details of section 1, and some expand on techniques described in section 2. This section finishes with discussions of "traditional" computerized tomography (CT) techniques followed by newer developments such as differential tomography, Compton tomography, coherent scatter tomography, and fluorescent X-ray tomography.

* On leave from the Instituto de Ciencias Nucleares, Universidad Nacional Autonoma de Mexico, Mexico City, Mexico.

1. Introduction

In the past two decades there has been an explosion of new analytical techniques in which keV photons have been used. These techniques have been developed by scientists working in a variety of disciplines, and as a result there often exists seemingly confusing and conflicting jargon to describe the same processes and techniques. Likewise, reports on the development of these techniques are scattered over tens if not hundreds of journals.

In particular, there are new points of view concerning the fundamental interactions, i.e., the photoelectric effect (PE), coherent scattering and incoherent scattering. The "traditional" treatments of these interactions employ simplistic approximations that should be regarded only as a starting point. These approximations are extremely widely used, partly because of their classical nature, and partly because they are extremely simple to use. They work to some extent in certain energy and angle regions, but cannot explain all interactions. Therefore, it is imperative that the end users understand the approximations and their inherent limitations in order to avoid abusing them. To give an example, the approach that led to the Thomson and Klein–Nishina (KN) formulas assumes the interaction of an electromagnetic wave is with a free electron. It is easy to realize that atomic elements are not free. The atomic form factor (AFF) and incoherent-scattering function (ISF) approach then simply provide fudge factors to the Thomson and KN formulas. The AFF and ISF have the most important impact on the actual cross section. Frequently both the Thomson and KN cross sections are introduced without stressing the fact that they are strongly dependent on the polarization of the incident photons. The reason is that the polarized sources have often been rare. With the recent growth in the availability of sources of polarized X-rays, it is important to review and "update" the physics of polarized X-rays, which was until now mostly of theoretical interest only. It is more logical to study the physics for unpolarized photons as a consequence of the physics for polarized photons.

The most famous and widely used X-ray technique is X-ray diffraction. This technique has long been studied and most of the details are readily available. Wavelength-dispersive (WD) X-ray fluorescence (XRF) is another traditional technique that will not be covered here. The "new" techniques developed in the past two decades, which will be discussed in this paper, include energy-dispersive (ED) XRF; photon-transmission method, which includes computed tomography (CT); and photon-scattering techniques, including Rayleigh to Compton ratios, Compton profile and scatter imaging.

The authors felt that a logical development of this review paper should start with a discussion of the fundamental interactions and some aspects of the progress achieved toward their knowledge (section 1). In section 2 non-imaging techniques will be discussed such as energy-dispersive XRF, scattering techniques, and Compton-profile techniques. In section 3 the progress in imaging techniques will be presented. There is overlap in the basic interactions utilized in the non-imaging and imaging techniques, however the break here is along the lines of the different technological approaches required for these two basic categories.

Summarizing the content of the paper, the theoretical background of photoelectric, coherent and Compton effects, with particular regard to polarized radiation, will be given in section 1. Some selected examples of how the general aspects of interaction of radiation with a specimen would help is given by X-ray fluorescence (XRF) and Compton-scattering techniques which will be described in section 2. In section 2.1, the angular distribution of secondary radiation will be depicted in many cases of practical interest. Further, the energy-dispersive X-ray fluorescence is described in detail in section 2.2. In section 2.3 the Compton-scattering techniques are described, and several examples of applications are given, with particular reference to the ratio of coherent to Compton radiation, which is independent of

the geometry. Several aspects of secondary radiation emitted by an irradiated sample are considered. No practical applications of XRF are given, because the technique is very well known.

In section 3, imaging techniques are described, in connection with the process of penetrating matter in a specimen by an incident beam of radiation (transmission tomography), or with the process of coherent Compton radiation. In the latter case, the secondary (scattered) radiation is in general collected at 90°, with respect to the incident beam. Finally, new possibilities of tomographic methods are described which refer to the use of two monoenergetic beams, which energy-bracket the energy of the photoelectric discontinuity of an element to be exalted (differential tomography), or to the spatial analysis of secondary fluorescent radiation (XRF tomography).

1.1. The photoelectric effect

The photoelectric effect is a two-step event in which (i) an electron from a inner shell (K, L, M, ...) is removed and subsequently (ii) an X-ray or an Auger electron (depending on the fluorescence yield) is emitted. The more loosely bound electrons require lower-energy radiation in order to eject them. As the exciting radiation energy is increased, we pass through jumps in the cross section known as absorption edges. These absorption edges result from an electron in a different orbital becoming available for PE absorption. The probability for electron-vacancy production in a particular orbital is greatest for photon energies immediately above the orbital's threshold for the ejection of the bound electron. The probability then decreases approximately as E^{-3}. This energy dependence has important consequences when one wishes to analyze a wide range of elements using a single-energy photon source. After the electron is ejected, the irradiated atoms will emit X-rays resulting from the decay of the excited states. Each element has a characteristic set of X-rays, the energy of which allows its identification. A sample containing several elements will emit as many X-rays of characteristic energies as there are elements. The intensity of these X-rays is approximately proportional to the elemental composition of the sample itself. The photoelectric effect is, therefore, the basic effect for the X-ray fluorescence analysis.

Each element deexcites with the emission of K_α and K_β X-rays with a constant intensity ratio. K_α rays results from the transition of an electron from the L- to the K-shell; K_β rays results from the transition from the M- to the K-shell. In a similar manner, when an electron of the L-shell is removed, the atom deexcites by emitting L_α, L_β and L_γ X-rays (transitions from the shells M, N, and O). The subscripts α, β, γ further refer to the subshells of the M, N, O electronic shells.

1.2. Scattering of keV photons by a single electron

The most "common" models for the scattering of X-rays by atoms starts with the assumption that the atomic cross sections can be calculated by multiplying the free-electron cross sections with a correction, which is equal to the number of electrons in an atom that is free to scatter either coherently or incoherently. The correction for the Rayleigh (coherent) scattering cross section is known as the atomic form factor and the simplest correction for the atomic Compton (incoherent) scattering cross section is known as the incoherent-scattering function. All of the atomic effects are included in these two corrections but the matrix effects, such as diffraction, must be accounted for separately. The atomic Compton scattering is further complicated with an energy distribution, which contains information on the matrix. Therefore, the scattering of X-rays by free electrons will be reviewed first, followed by a review of the scattering by bound electrons.

X-rays and gamma rays are electromagnetic radiation and as such have electric field, or polarization, vectors e associated with them. These vectors are normal to the propagation vectors k (fig. 1a). The propagation vectors have the direction of propagation, and depend on the photon energy E; $k = E/c - h/\lambda - h\nu/c$ (where λ is the wavelength and ν the frequency). Since the vectors e are normal to the vectors k, the vectors k act as an axis about which the vectors e are oriented. There is an infinite set of directions about k that the e vectors can assume.

If a beam of photons has a net orientation of the e vectors, then the beam is said to be polarized. If the orientation can be described as a linear superposition of e vectors, the beam is said to be linearly polarized (fig. 1a). Linear polarization requires the absence of variation in the net e vector projections as a function of time or space. If there is no net polarization of the beam, it is said to be unpolarized. Unpolarized radiation requires that there are equal projections of the e vectors on any two arbitrary perpendicular planes (fig. 1b). This concept is important since we have now established that the physics for unpolarized radiation and the mathematical development can always start with the discussion of polarized radiation. For most sources of X-rays, the assumption of linear polarization is valid.

In order to start our discussion, we need to assume the electron is not only free, or quasifree, but is also at rest. We can now present two simple models: (1) the Thomson scattering which is a coherent dipole interaction, meaning no loss of photon energy or change of phase, and (2) the Compton scattering which is an incoherent elastic event in which a fraction of the photon energy is imparted to the electron. This is a source of confusion since the atomic Compton scattering (by a bound electron) is an inelastic event as far as the atom is concerned, even though the kinematics is derived for an elastic process, which is inherent to the quasifree assumption. Since there is no energy transfer in the coherent-scattering process, there are no effects from the relative motion of the electrons, in contrast to the case of atomic Compton scattering.

The incoherent scattering of X-rays by a quasifree electron can be derived with conservation of momentum and energy. However, because of the "mass differences", the electron can never accept all of the energy of the photon, so the photon can never be absorbed by a free electron. This is why there is no free electron equivalent to the photoelectric effect.
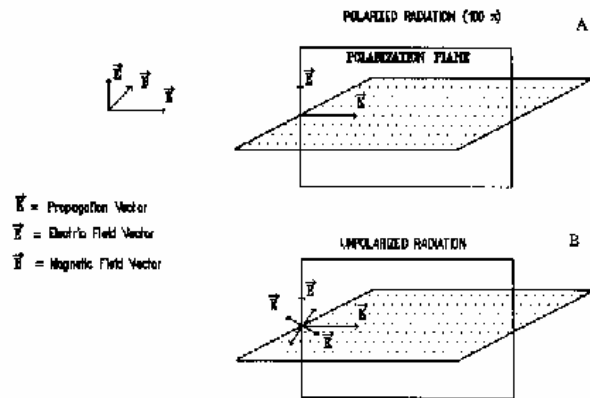

Fig. 1. Models of electric field vector e and propagation vector k for the scattering of X-rays.

1.2.1. The Thomson cross section

First we will introduce the Thomson cross section which can be understood as a dipole interaction of a polarized electromagnetic wave with a stationary free electron. The interaction can be seen as the elastic scattering of a ball on a wall, the ball changes its direction (momentum), but not its energy. If we now add a large degree of spin to the ball, as in a gyroscope, the probability for the scattering will be dependent on the orientation of the spin axis before and after the scattering event. In the case of an X-ray scattering into $d\Omega$ the probability is given by the scalar product of the electric field vectors of the incident (e_0) and scattered (e) X-rays,

$$d\sigma/d\Omega = r_0^2 \cos^2\alpha , \quad \cos\alpha = e_0 \cdot e , \tag{1}$$

where r_0 is the classical electron radius. It is difficult to visualize the scattering geometry as a function of the angle α, but it is relatively easy to visualize it as a function of the scattering angle θ. The scattering angle is the angle between the propagation vectors of the scattered and incident photons $\cos\theta - k \cdot k_0$. If we want to express the cross section as a function of θ, we start by considering the case of an X ray-beam 100% polarized. The probability of scattering in such a way that the e vectors are found in a plane perpendicular to e_0 (fig. 2a) is

$$(d\sigma/d\Omega)_{Th,\perp} = r_0^2 , \tag{2}$$

and this scattering is isotropic in this plane.

If the scattering plane coincides with the plane of the polarization, the cross section becomes (fig. 2b)

$$(d\sigma/d\Omega)_{Th,\parallel} = r_0^2 \cos^2\theta . \tag{3}$$

Finally, if the X-ray beam is unpolarized, there is an equal probability of any incident e_0 orientation and the probability of scatter is half the sum of eqs. (2) and (3) (fig. 2c),

$$(d\sigma/d\Omega)_{Th} = \tfrac{1}{2}r_0^2(1 + \cos^2\theta) . \tag{4}$$

1.2.2. The degree of polarization

Now that we have seen the effects that polarization has on the scattering of X rays, we need to introduce the definition of degree of polarization noting that we restrict the discussion throughout this paper to the problem of linearly polarized X-rays. It is reasonable to define two perpendicular planes, one parallel to e_0 (hence the parallel plane) and the other perpendicular to e_0. The fraction of projections onto the parallel plane is defined as $P_\parallel$ and the fraction of projections onto the perpendicular plane is defined as $P_\perp$. For linearly polarized photons the cross section is then

$$d\sigma/d\Omega = P_\parallel(d\sigma/d\Omega)_\parallel + P_\perp(d\sigma/d\Omega)_\perp . \tag{5}$$

The degree of polarization is usually defined as

$$P = (P_\parallel - P_\perp)/(P_\parallel + P_\perp) . \tag{6}$$

P is 1 if the photons are 100% polarized and the observation is in the plane of polarization. P is 0 for unpolarized X-rays, and is -1 if the observation is in the perpendicular plane.
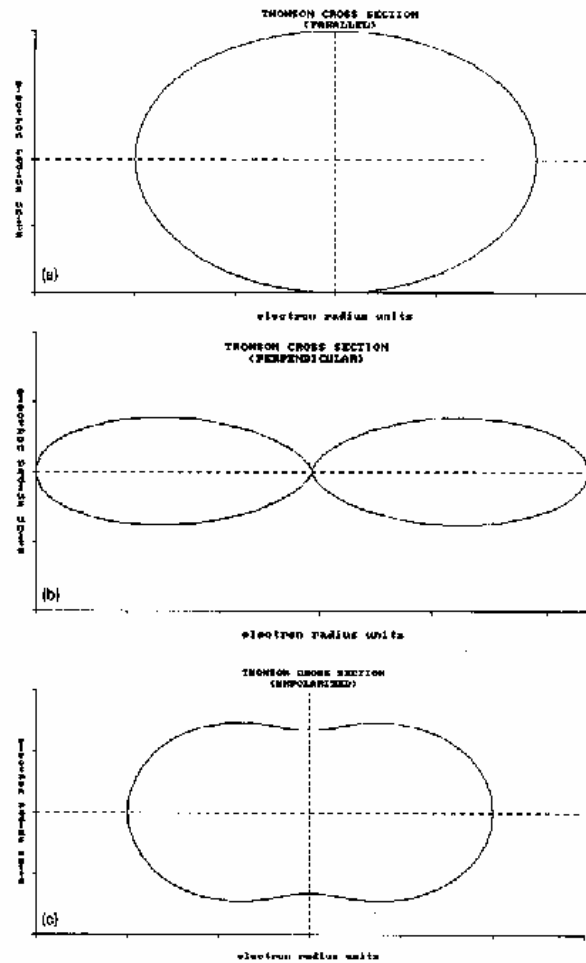
electron, the photon changes phase, and the electron gains kinetic energy; this is the main difference with coherent scattering. Hence the interaction cannot be completely dipole in nature, and we will lose some of the polarization information, as compared to coherent scattering. The Klein–Nishina formula for the scattering of an individual photon can be written as

$$(d\sigma/d\Omega)_{KN} = \tfrac{1}{4}r_0^2(K/K_0)^2(K/K_0 + K_0/K - 2 + 4\cos^2\alpha) , \tag{7}$$

$$K/K_0 = [1 + \gamma(1 - \cos\theta)]^{-1} , \quad \gamma = E_0/m_0c^2 . \tag{8}$$

As in Thomson scattering, the $\cos^2\alpha$ term contains all of the polarization information whereas the term $K/K_{\parallel} + K_{\parallel}/K - 2$ accounts for part of the scattered radiation being unpolarized. Hence it is sometimes referred to as the "depolarization term". With the exception of the contributions from the depolarization terms, the angular distribution is similar to that of Thomson scattering. In general, the depolarization terms are small, but they can dominate when highly polarized photons are scattered into 90°.

In the low energy limit $K/K_0 \to 1$, the Klein–Nishina cross section is equal in magnitude to the Thomson cross section. Since the energy of the photon is proportional to the magnitude of the propagation vector, k, the ratio of the energy of the Compton-scattered photon, E, to the incident energy, E_0, is the same as K/K_0. The Klein–Nishina formula for perpendicularly polarized radiation [equivalent to eq. (2)] is (fig. 3a)

$$(d\sigma/d\Omega)_{KN,\perp} = \tfrac{1}{4}r_0^2(K/K_0)^2(K/K_0 + K_0/K + 2) \tag{9}$$

and the Klein–Nishina formula for parallel polarized radiation [equivalent to eq. (3)] is (fig. 3b)

$$(d\sigma/d\Omega)_{KN,\parallel} = \tfrac{1}{4}r_0^2(K/K_0)^2(K/K_0 + K_0/K - 2 + 4\cos^2\theta) . \tag{10}$$

The Klein–Nishina formula for unpolarized radiation [equivalent to eq. (4)] is (fig. 3c)

$$(d\sigma/d\Omega)_{KN} = \tfrac{1}{2}r_0^2(K/K_0)^2(K/K_0 + K_0/K - \sin^2\theta) . \tag{11}$$

1.3. Scattering of keV photons by bound electrons

1.3.1. Rayleigh scattering

Rayleigh scattering is the coherent interaction of photons with bound electrons. Even though there are other components to the total coherent scattering, such as nuclear Thomson, Delbruck, and resonant nuclear scattering, Rayleigh scattering is the only significant coherent event for keV photons. As depicted in the Thomson scattering, the energy and phase of the scattered photon is the same as of the incident photon.

Many different theoretical approaches have been presented in the past few years to describe Rayleigh scattering [2–5]. The most commonly used and simplest approach is to consider the coherent scattering as a modification, with an atomic form factor $F(q, Z)$, of the Thomson cross section,

$$(d\sigma/d\Omega)_R = F^2(q, Z)(d\sigma/d\Omega)_{Th} , \quad q = (\sin\tfrac{1}{2}\theta)/\lambda , \tag{12}$$

Fig. 2. Polar plot for differential cross section for Thomson scattering. (a) 100% polarized photons with e vector perpendicular to the scattering plane, (b) 100% polarized photons with e vector parallel to the scattering plane, (c) unpolarized photons.

1.2.3. The Klein–Nishina cross section

As the basis for incoherent scattering we will introduce the Klein–Nishina cross section. This cross section was derived assuming: (1) the electrons are quasifree (conservation of energy and momentum), hence neglecting binding effects of the electrons; (2) the electrons are at rest, and (3) the X-rays are linearly polarized [1]. In incoherent scattering an X-ray photon imparts some of its energy to the

Klein-Nishina differential cross section
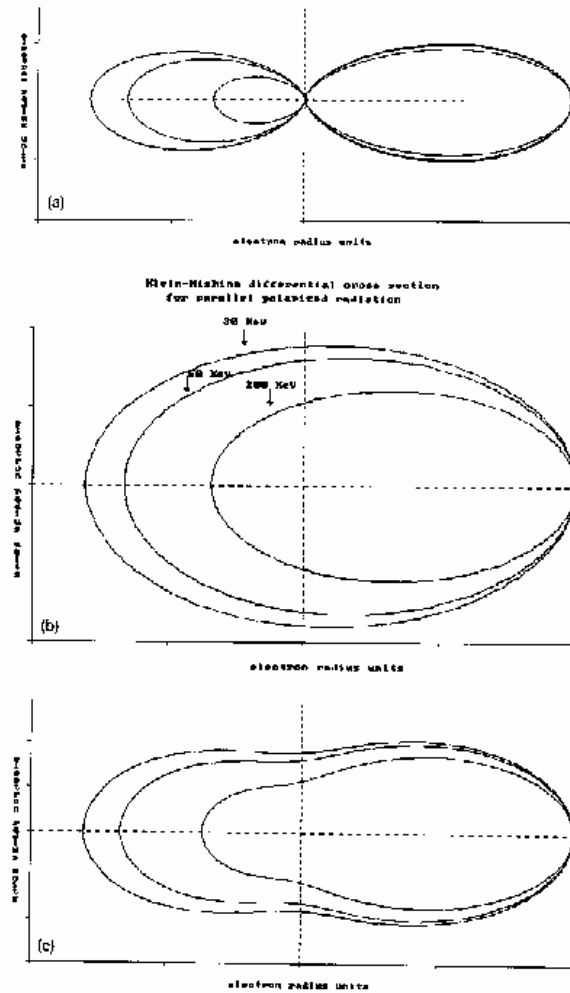for parallel polarized radiation

Fig. 3. (a) Klein–Nishina differential cross section for perpendicularly polarized radiation. (b) Klein–Nishina differential cross section for parallel polarized radiation. (c) Klein–Nishina differential cross section for unpolarized radiation. Plots (a), (b), (c) were calculated for 30, 60, 200 keV photons.

where q is the momentum transfer. Due to the simplicity of this approach, a tremendous effort has been centered on methods for calculating $F(q, Z)$. One method to calculate $F(q, Z)$ is to use the total charge density $\rho(r, Z)$ of the atom calculated from Hartree–Fock [6, 7] wave functions having summed

over all orbitals,

$$F(q, Z) = 4\pi \int_0^\infty r^2 \rho(r, Z) \frac{\sin(qr)}{qr} dr. \tag{13}$$

These calculations usually assume a free atom (or ion) [6, 7] with a spherically symmetric electron charge distribution and hence include no chemical or matrix effects.

The magnitude of the form factor when $q = 0$ is equal to Z. It is then a monotonically decreasing function to 0 as $q \to \infty$. Therefore, Rayleigh scattering is strongly peaked forward. The experimental results available are usually in good agreement with the theoretical predictions except for elements with high Z where the discrepancies are sometimes large. It should be pointed out that, as the momentum transfer increases, the form factors rapidly become small. The relative magnitude of this decrease, specially for low-Z elements (i.e., $Z < 6$), is strongly dependent on Z [8]. This behaviour makes coherent scattering attractive for applications, because of the sensitivity to the effective Z of the sample. Unfortunately, it should be stressed that this strong dependance happens only when the cross section is greatly reduced.

Since $F(q, Z)$ has been defined as a single-parameter function, it cannot predict problems associated with absorption edges, known as anomalous scattering. Around the absorption edges the cross section rapidly varies with energy. One method to account for the absorption edges is to replace $F(q, Z)$ with

$$f(q, Z) = F(q, Z) + f' + f''. \tag{14}$$

Attempts are then made to calculate and measure f' and f'' [9–17]. At low momentum transfer q, there are strong interference effects due to the spatial distribution of the electrons in ordered structures, as a function of q. From an experimental point of view, the anomalous form factor can be determined with interferometric measurements [10, 11].

1.3.2. Atomic Compton scattering

In the atomic Compton scattering of a photon by bound electrons, we can observe two main features: (i) the ejection of electrons by providing enough energy to remove them from their orbitals; and (ii) the broad spectral distribution of the scattered photons, which is related to the momentum distribution of the electrons. The energy loss suffered by the photon is $\Delta E = E_0 - E$, where E_0 and E are the energies of the incident and scattered photons, respectively. This energy ΔE, minus the binding energy (BE), is the kinetic energy (KE) of the electron. This statement means that (1) the atomic Compton scattering requires $\Delta E > BE$ and (2) the momentum distribution of the target electrons and the energy distribution of the scattered photons are interdependent. Conversely, the measurements of the energy distribution of the scattered photons and scattered electrons in coincidence allow the determination of the electron orbitals of emitted electrons and scattered photons in coincidence allow the determination of the electron orbitals involved in the scattering. As one tries to use the incoherent scattering function, one should never forget that the Klein–Nishina model assumes for all electrons $E \gg BE$ and $S = Z$. With keV photons the situation $S \ll Z$ arises frequently and then the assumption is not valid.

In most analytical techniques using scattering radiation, we are not as interested in the ejected electrons as much as we are in the scattered photons, so we will limit the discussion only to scattered electrons and scattered photons. The Klein–Nishina cross section was derived per electron free to scatter. If the energy and momentum transfer are high enough so that all scattering events are incoherent, then the atomic

Compton cross section is $Z(d\sigma/d\Omega)_{KN}$. The simplest approximation to the atomic Compton scattering cross section is the incoherent-scattering function approximation,

$$(d\sigma/d\Omega)_c = S(q, Z)(d\sigma/d\Omega)_{KN} . \tag{15}$$

The term $S(q, Z)$ is the incoherent-scattering function equivalent to $F(q, Z)$ for Rayleigh scattering. In the Rayleigh cross section $F(q, Z)$ is squared due to the coherence of the scattering. Like $F(q, Z)$, the magnitude of $S(q, Z)$ ranges from 0 to Z, but to a first-order approximation, they are complementary (or competing) functions,

$$S(q, Z) + F(q, Z) = Z . \tag{16}$$

Therefore, $S = 0$ when $q = 0$ and $S = Z$ as $q \to \infty$. Like tables for the atomic form factors, tables of incoherent-scattering functions have been generated and are readily available in the literature [18-20]. The incoherent-scattering function approximation is certainly the simplest and most widely used method of calculating differential scattering cross sections, however, numerous other approximations to the atomic Compton cross sections are available [21, 22].

There are two effects that cannot be predicted with this approach: (i) the energy distribution of the scattered photons, which results from the momentum distribution of the bound electrons; and (ii) the anomalous incoherent scattering. The energy distribution of the atomic Compton spectrum is characterized by two concomitant features. The first is the shift of the atomic Compton spectrum towards a lower energy (eq. 8) at larger scattering angles, and the second is the broadening of the photon spectrum due to the momentum distribution of the electrons (known as the Compton profile) in the target. In order to calculate this energy spread, we must use a double differential cross section such as the impulse approximation [23-25],

$$d\sigma/d\Omega\, dE' = \tfrac{1}{2}m_0 r_0^2(E^2 + E'^2 - 2E'E \cos \theta)^{1/2}(E'/E_0)(E'/E_0 + E_0/E' - \sin^2\theta)J(p_z, Z) . \tag{17}$$

E is the mean photon energy, and E' is the incremental energy about E. The term $J(p_z, Z)$ is the Compton profile and p is the component of the momentum along the direction of the incident beam. Tables of Compton profiles (momentum distribution) have been generated from Hartree-Fock and relativistic Dirac-Hartree-Fock functions from the momentum distribution, $\rho(p)$, for the electrons from all orbitals of all atoms [26]. These calculations assume that the distribution does not depend on the direction of observation,

$$J(p_z, Z) = 2\pi \int_{p_z}^{\infty} p\rho(p, Z)\, dp . \tag{18}$$

The relation between p_z and the incremental energy E' is

$$p_z = \tfrac{137}{511}[EE'(1 - \cos \theta) - m_0 c^2(E - E')]/(E^2 + E'^2 - 2EE' \cos \theta)^{-1/2} . \tag{19}$$

As before the impulse approximation is not the only method for calculating the double differential scattering cross section [27-29], but is the simplest.

Thus an entire field of Compton profile measurements has evolved. The momentum distributions are determined by measuring changes in the atomic Compton spectra against a reference sample or a theoretical calculation [30-39]. However, the electronic states are modified by the chemical and matrix effects, these effects cannot be accounted for separately as was the case with Rayleigh scattering. External fields will also affect the distributions and when present must be included in the calculations [40-43]. The Compton scattering distribution is further complicated by the fact that it is non-gaussian in shape. This may seem odd at first, since the Compton profiles from all orbitals are themselves close to being gaussian in shape. However, the total profile is a sum (and not a convolution) of the contributions from each orbital [44]. The deviation from a gaussian distribution can be observed experimentally when the resolution of the detector is good (state of the art solid state detectors) and when the collimation is sufficiently narrow to avoid geometrical effects [46].

1.3.3. Summary of differential cross sections

(a) The low energy limit of the Klein-Nishina cross section is the Thomson cross section. (b) The atomic form factors and the incoherent-scattering functions are defined as the ratio of Rayleigh and atomic Compton scattering cross section to the Thomson and Klein-Nishina cross sections, respectively. It is then claimed that $F(q, Z)$ and $S(q, Z)$ can be calculated from atomic wave functions. (c) The total number of electrons available for a scattering event is fixed (equal to Z per atom) and in this sense the coherent and incoherent interactions are competing events. (d) When the energy and momentum transfer is too small to move an electron, the scattering can only be coherent. (e) The Rayleigh scattering is strongly peaked forward (small q) and the atomic Compton scattering is dominant in the backward directions (large q); in fact, the atomic Compton cross section is zero at 0° (see also figs. 4-10).
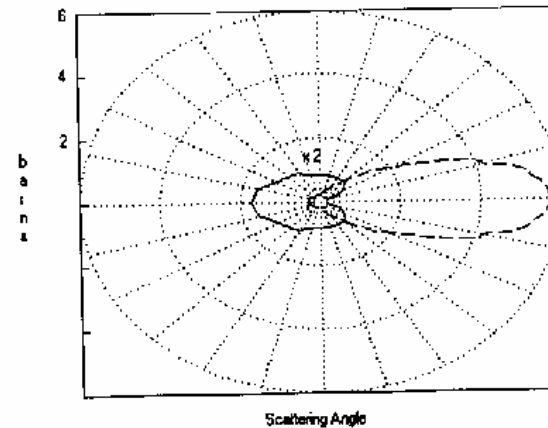

Fig. 4. The differential cross section for coherent (dotted line) and Compton scattering of unpolarized radiation in water, at $E_c = 10$ keV.
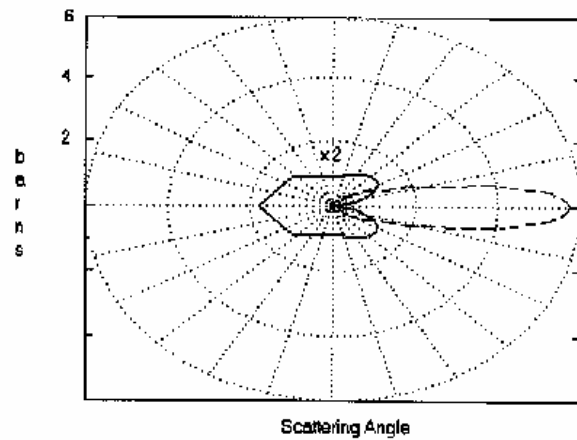
Fig. 5. The differential cross section for coherent (dotted line) and Compton scattering of unpolarized radiation in water, at $E_0 = 20$ keV.
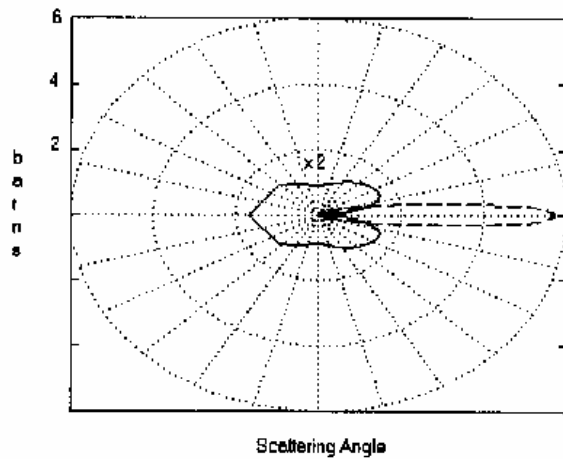

Fig. 6. The differential cross section for coherent (dotted line) and Compton scattering of unpolarized radiation in water, at $E_0 = 40$ keV.

The atomic form factor and incoherent-scattering function approximation to the calculation of differential cross sections has the merit of simplicity, but care must be exercised to ensure validity in certain energy and angle ranges [18, 46, 47]. It assumes that, for a given element, the correction is dependent only on a single parameter, q, the momentum transfer between the photon and the target
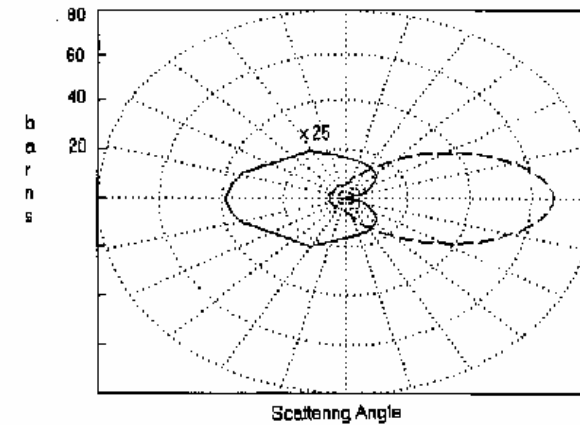
Fig. 7. The differential cross section for coherent (dotted line) and Compton scattering of unpolarized radiation in a copper foil, at $E_0 = 10$ keV.
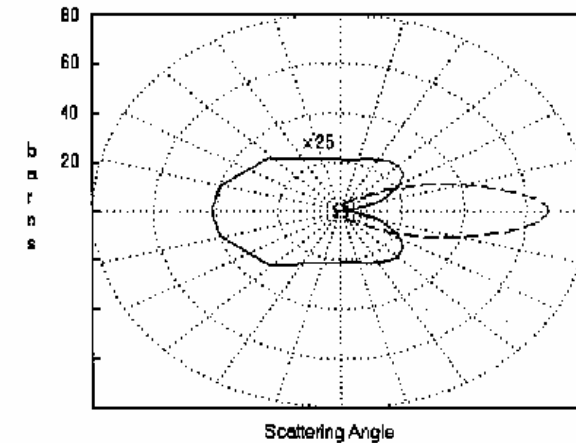

Fig. 8. The differential cross section for coherent (dotted line) and Compton scattering of unpolarized radiation in a copper foil, at $E_0 = 20$ keV.

electron. Problems of accuracy in specific ranges of q may not be obvious from the tables of total cross sections and attenuation coefficients since in those tables the coefficients are integrated over all angles.

1.3.4. Angular distribution of secondary radiation

Peaks from the photoelectric effect and from coherent and incoherent scattering are in general visible at all angles around the sample, with an intensity which is proportional to the differential cross
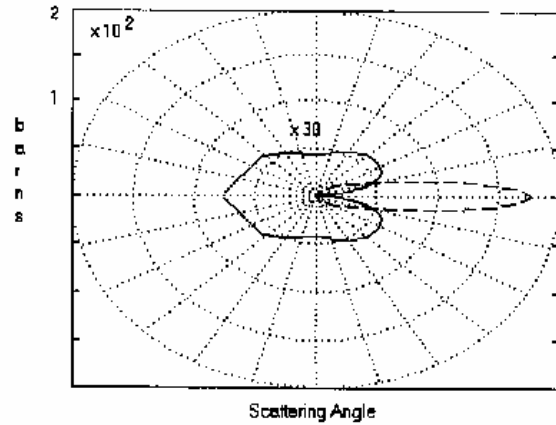
Fig. 9. The differential cross section for coherent (dotted line) and Compton scattering of unpolarized radiation in a silver foil, at $E_0 = 40$ keV.
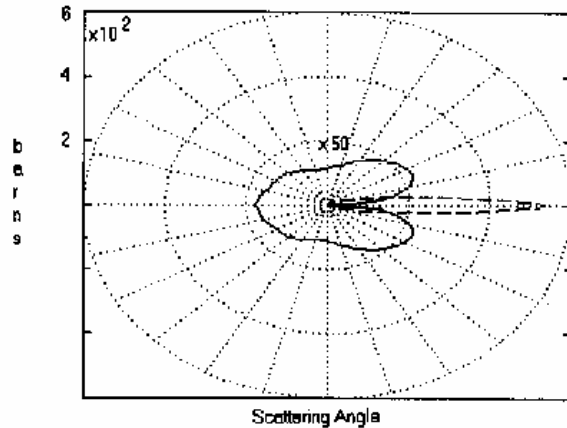

Fig. 10. The differential cross section for coherent (dotted line) and Compton scattering of unpolarized radiation in a lead foil, at $E_0 = 100$ keV.

sections (see figs. 4–10). It is also very important to plot the distribution of the differential cross sections for all effects as a function of incident (monoenergetic) radiation and of the specimen material. In figs. 4–10 the differential cross sections are shown for $E_0 = 10, 20, 40$ keV for a water matrix, $E_0 = 10$ and 20 keV for copper, $E_0 = 40$ keV for silver and $E_0 = 100$ keV for lead.

The Compton and coherent cross sections have been calculated from eqs. (12) and (15). The atomic form factor $F(q, Z)$ and the incoherent-scattering function $S(q, Z)$ were from the tables of Hubbell et

al. (figs. 11 and 12) [18, 47]. In fig. 13, the theoretical atomic form factor $F(q, Z)$ of water is plotted versus q, and compared with the experimental data deduced from the diffraction measurements of Kosanetzky et al. [48].

1.3.5. Total cross sections

The total scattering cross sections, which are used to generate tables of attenuation coefficients of photon beams, are calculated by integrating the differential cross section over all angles,

$$\sigma = \int_{4\pi} \frac{d\sigma}{d\Omega} \, d\Omega .$$

Since the differential cross sections are strongly dependent on angle, only in specific energy regions can we make the assumption of integrating the Thomson or Klein–Nishina cross section over all angles and then multiplying it by an effective form factor or effective incoherent-scattering factor. Therefore, the tables of total cross sections are usually calculated with numerical integrations over 4π [18, 45]. For the calculation of the Rayleigh cross section, the atomic form factors have been fitted to nine-parameter exponentials [6, 7]. These were used to generate the coherent scattering cross sections in the McMaster tables [45]. However, it has been shown that with the nine-parameter function the total cross section can be integrated analytically [49].
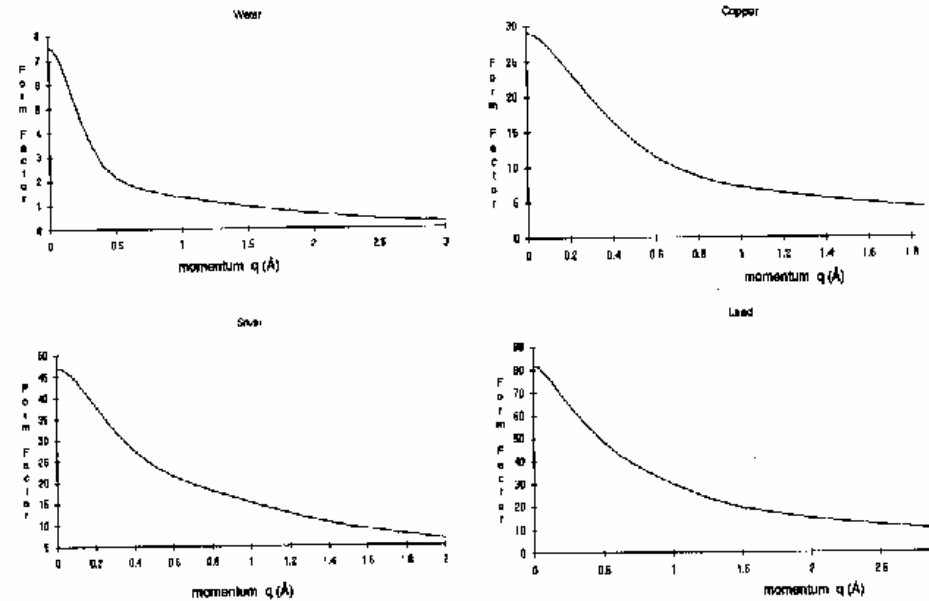

Fig. 11. Atomic form factor $F(q, Z)$ versus momentum q for $Z = 7.5$ (water), $Z = 29$, $Z = 47$ and $Z = 82$; theoretical values from Hubbell and Øverbø [47].
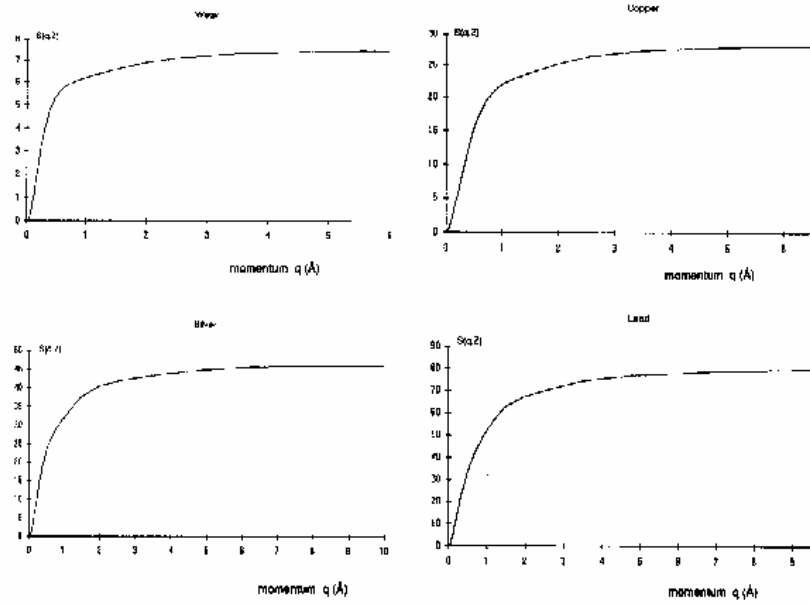
Fig. 12. Incoherent scattering function $S(q, Z)$ versus momentum q for $Z = 7.5$ (water), $Z = 29$, $Z = 47$ and $Z = 82$. Theoretical values from Hubbell et al. [18].
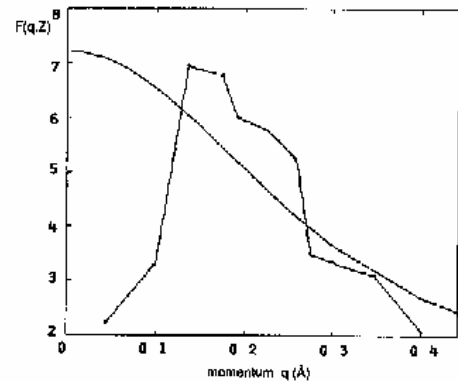

Fig. 13. Theoretical atomic form factor $F(q, Z)$ of water (continuous line) and experimental values (·) deduced from the measurements of Kosanetzky et al. [48].

1.3.6. Integration of cross sections over detector solid angle

The angular dependence of the scattering cross sections is complicated since both the Thomson and Klein–Nishina and the scattering factors exhibit angular dependence. The angular dependence becomes more pronounced as the beam of X-rays becomes polarized. If the observation of scattering is made in the plane of polarization of a highly polarized beam of X-rays, the cross section for scattering into a detector solid angle of $d\Omega_D$ cannot be approximated as

$$\sigma_0 = C(d\sigma/d\Omega)\,d\Omega_D , \tag{20}$$

where C is a representative value for either $F(q, Z)$ or $S(q, Z)$. Therefore, considerable effort has been put in the past few years into integrating eqs. (12) and (14) over the solid angle of a circular detector without resorting to Monte Carlo methods [50–52, 54, 55].

The efforts to integrate the cross sections can be summed up in two equations. The integrated cross section for Rayleigh scattering is [54]

$$\sigma_R = \pi r_0^2 F^2(q, Z)[(1 - H^2)(\tfrac{4}{3} - \tfrac{1}{3}\cos^3 t - \cos t) + 2H^2(\tfrac{2}{3} + \tfrac{1}{3}\cos^3 t - \cos t)] , \tag{21a}$$

and for the atomic Compton scattering [54]

$$\sigma_{a,C} = A + B , \quad A = \pi r_0^3 S(q, Z)(1 - \cos t)(K/K_0)^2(K/K_0 + K_0/K - 2) ,$$
$$B = \pi r_0^2 S(q, Z)(K/K_0)^2[(1 - H^2)(\tfrac{4}{3} - \tfrac{1}{3}\cos^3 t - \cos t) + 2H^2(\tfrac{2}{3} + \tfrac{1}{3}\cos^3 t - \cos t)] . \tag{21b}$$

The functions $F(q, Z)$, $S(q, Z)$ and K/K_0 are all evaluated at the nominal scattering angle θ. The parameter, t, is the detector aperture aspect ratio: $t = \arctan(r/R)$, where r is the aperture radius and R is the distance from the point of scatter to the aperture. The value of H is determined from the position of the detector with respect to both the propagation $\cos\theta$ and the polarization $\sin\psi$ of the X-rays [54], $H = \cos\theta\sin\psi$. This fact illustrates the interdependence of detector position and polarization.

Equations (21a) and (21b) require the assumptions: (i) the atomic form factor and incoherent-scattering function approximations are valid; (ii) the radiation is linearly polarized (which includes the case of unpolarized radiation); (iii) the detector aperture is small enough that $F(q, Z)$, $S(q, Z)$ and K/K_0 are odd functions around θ over Ω_D.

1.4. Absorption and attenuation of keV photons

When a beam of monoenergetic photons with energy E_0 and photon flux density (number of photons per unit area and time) N_0 crosses a homogeneous absorber of thickness x, the emerging photon flux density N is given by

$$N = N_0 \exp[-\mu(\rho, Z, E_0)x] , \tag{22a}$$

where μ (cm^{-1}) is the linear attenuation coefficients for material of physical density ρ (g/cm^3) and atomic number Z. Implied in eq. (22a) that x is "thin" enough so that multiple interactions are not probable.

For energy values greater than about 10 keV, when molecular binding energies are small, it is a

reasonable approximation to assume that μ is directly proportional to the physical density and write

$$N - N_0 \exp[-\mu(Z, E)/\rho]\, \rho x \, . \tag{22b}$$

where $\mu(Z, E)/\rho$ is the mass attenuation coefficient (in cm^2/g). The quantity μ/ρ is related to the probability (or cross section) that radiation will interact with matter in some manner. Each interaction is assumed to "remove" a photon from the beam even though a scattering event does not absorb the photon. This probability may be thought of as a measure of the area of the atom subject to the radiation interaction mode in question.

The attenuation coefficient gives a measure of the total absorption of the radiation which passes through any material, regardless of the interaction mode. Since there are three primary interaction modes, photoelectric (ph), Compton (C) and coherent (coh), μ/ρ can be written as

$$\mu/\rho = (\mu/\rho)_{ph} + (\mu/\rho)_C + (\mu/\rho)_{coh.} \, . \tag{22c}$$

The contribution of three effects, separately, as a function of energy, for lead ($Z = 29$) and soft tissue ($\bar{Z} \approx 7.5$) are shown in fig. 14. The photoelectric absorption edges for lead (L- and K-absorption edges) are also shown. One of the most widely used tabulations of μ/ρ are the McMaster tables [45].
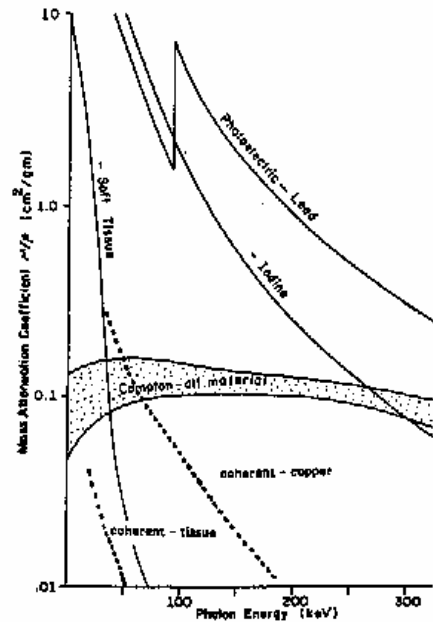

Fig. 14. Photoelectric mass-attenuation coefficient of lead, iodine and soft tissue. Compton mass-attenuation coefficient for all materials and coherent mass-attenuation coefficient for copper and soft tissue.

2. Analytical applications

2.1. Introduction

As was discussed in section 1, when a specimen is irradiated by photons, part of the radiation is absorbed through the photoelectric effect, part of it is coherently or incoherently scattered and part of it traverses the sample without interacting. When detectors are placed at various angles around the irradiated sample, photons can be collected and analyzed due to the various interacting processes. The energy and intensity of the various photon peaks will reflect the single process and its different cross sections (fig. 15). Useful analytical information about the specimen can be therefore deduced directly through the characteristic X-rays emitted by the elements constituting the specimen. Analytical information can also be indirectly deduced through the energy (for Compton effect) and/or intensity of scattered radiation.

For a monochromatic beam of photons, the spectrum will contain: (a) only a peak of energy E_0 and intensity $I_0 \exp(-\mu x)$ in the transmission mode; (b) a peak of energy E_0 due to elastic scattering by the sample; (c) a peak of energy E_C due to atomic Compton scattering by the sample; (d) peaks of various energies due to the photoelectric effect, which are characteristic of elements in the sample.

Figure 16 shows a typical spectrum, containing peaks of the type b, c and d, obtained by irradiating a silver foil with 59.6 keV photons and collecting the spectrum at 150° [57]. The detected spectrum is complicated by two effects: (1) the preferential removal of photons from a specific spectral region due to the absorption in the sample (self-absorption); (2) the generation of secondary radiation due to multiple interaction. These multiple interactions may be due to multiple scattering, multiple photoelectric interaction or mixture of scattering/photoelectric interactions. The self-absorption is treated in section 2.2 in relation to XRF techniques whereas multiple interactions are reviewed within the present section.
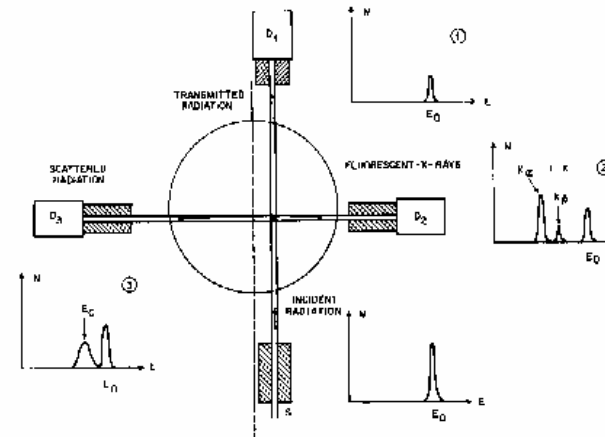

Fig. 15. Interaction of monoenergetic radiation with matter (cylindrical sample) and resulting X-ray spectra at 0° and 90°, showing transmitted spectrum (composed of a peak of E_0 = incident energy) and scattered spectrum (composed of a coherent-scattering peak of energy E_0) a Compton-scattered peak of energy E_C and X-rays peaks of energy depending on the emitting elements.
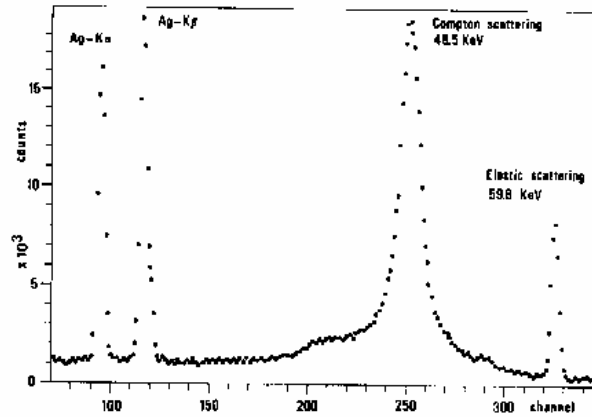
Fig. 16. Typical spectrum obtained by irradiating a silver foil with 59.6 keV photons and collecting the secondary photons at 150°. The Ag–K peaks and the Compton (48.5 keV) and elastic scattered peak (56.6 keV) are shown (from Cesareo [57]).

The system has an energy resolution, which determines how close two peaks can lie and still be distinguished. For most X-ray spectra this resolution is dominated by the detector. The atomic Compton distribution is further complicated by the fact that it is inherently broad. The energy broadening is determined by several factors: (a) geometry-dependent factor; (b) momentum distribution of the electrons in the scatter; (c) multiple-interaction processes.

(a) *Geometry-dependent factor.* The relation between primary energy (E_0) and Compton-scattered photon energies (E_C), is dependent on both the incident energy and angle θ,

$$E_C = E_0[1 + \gamma(1 - \cos \theta)]^{-1}, \tag{23}$$

in which $\gamma = E_0/m_0 c^2$. Figure 17 illustrates the relationship between E_0 and E_C. The range of accepted scattering angles $\Delta\theta = \theta_{max} - \theta_{min}$ gives rise to a "geometrical" G energy broadening of the scattered peak. One approximation for ΔG is

$$\Delta G = E_0[1 + \gamma(1 - \cos \theta_{max})]^{-1} - E_0[1 + \gamma(1 - \cos \theta_{min})]^{-1}. \tag{24}$$

The energy broadening is determined by both $\Delta\theta$ and the primary photon energy E_0. Figures 18a, b, c show ΔG for $\Delta\theta = 1°$, $2°$, $3°$ and $5°$, assuming θ_{min} and θ_{max} to be symmetrically distributed around $\theta = 45°$, $90°$ and $150°$.

(b) *Momentum distribution of the electrons in the scatterer.* If the momentum distribution of the electrons in the scatterer was the only factor degrading the energy resolution, the FWHM of the pulse height distribution ΔC would be
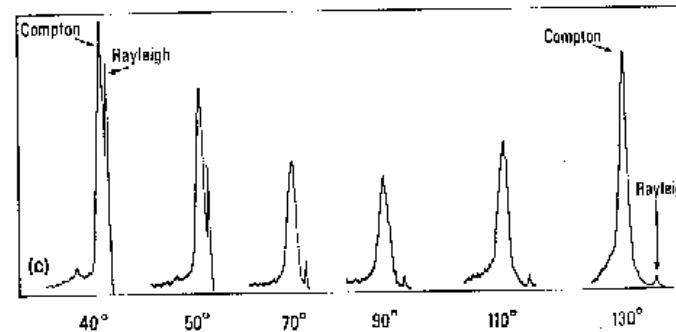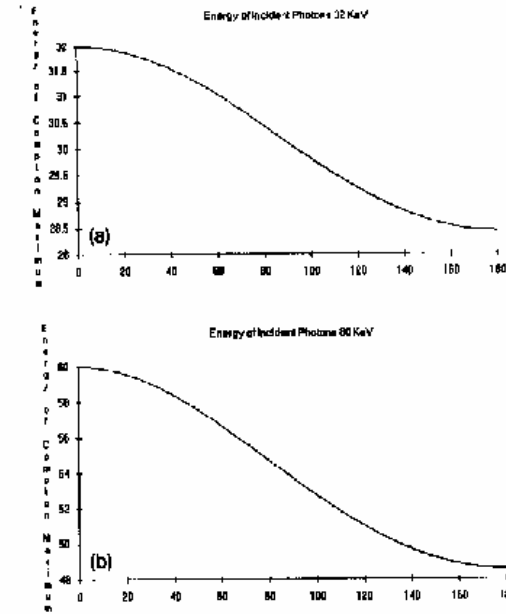
$$\Delta C \propto J(p_z, Z), \tag{25}$$

Fig. 17. Energy of Compton scattered photons versus scattering angle θ for incident energy of (a) 32 keV and (b) 60 keV. Scattered spectra produced in a low atomic-number target by 60 keV γ-rays at various angles and detected with a high resolution solid state detector are also shown (c).

in which p_z has been defined in section 1.3 and $J(p, z)$ is known as the "Compton profile". It can be determined from the distribution if the other factors can be assumed to be constant. From tables of $J(p_z, Z)$ (see for example ref. [28]), the Compton profile can be calculated. The effects of the Compton profile have been studied in several materials by Matschenko et al. [58] using the cited $J(p_z, Z)$ tables.
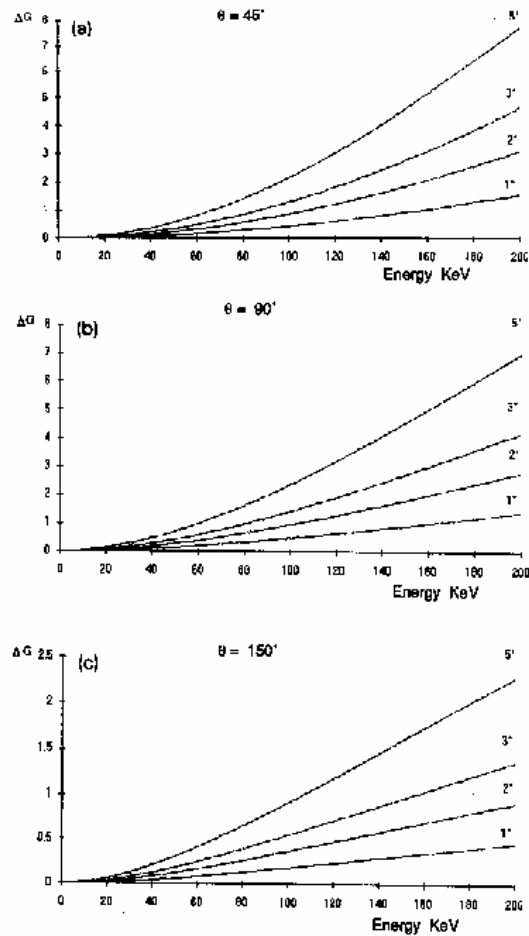
Fig. 18. The full width at half maximum of the Compton broadening ΔG for $\Delta\theta = 1°$, $2°$, $3°$ and $5°$ assuming $\Delta\theta$ to be symmetrical around $\theta = 45°$, $90°$, $135°$ and $180°$.

Fig. 19. (a) FWHM values of the Compton broadening ΔC due to Compton profile, for a scattering angle $\theta = 90°$, for beryllium, aluminium, polyethylene and lucite, as a function of primary photon energy E_0 (after data of Matschenko et al. [58]). (b) Calculated Compton profile for atomic hydrogen, carbon, and sodium normalized to one electron from Gatti et al. [59]. (c) Comparison of the Compton profiles for atomic carbon, ethane gas and diamond dust from Gatti et al. [59].

Figure 19a shows the FWHM value of the Compton broadening ΔC for a scattering angle $\theta = 90°$ and for beryllium, aluminum, polyethylene lucite, as a function of primary photon energy E_0.

A detailed analysis of the Compton profile from a practical point of view has been carried out by Gatti et al. [59] in order to study the possibility of correlating by means of a new tomographic device, the chemical properties of a region of tissue inside the human body, with the profile of the Compton
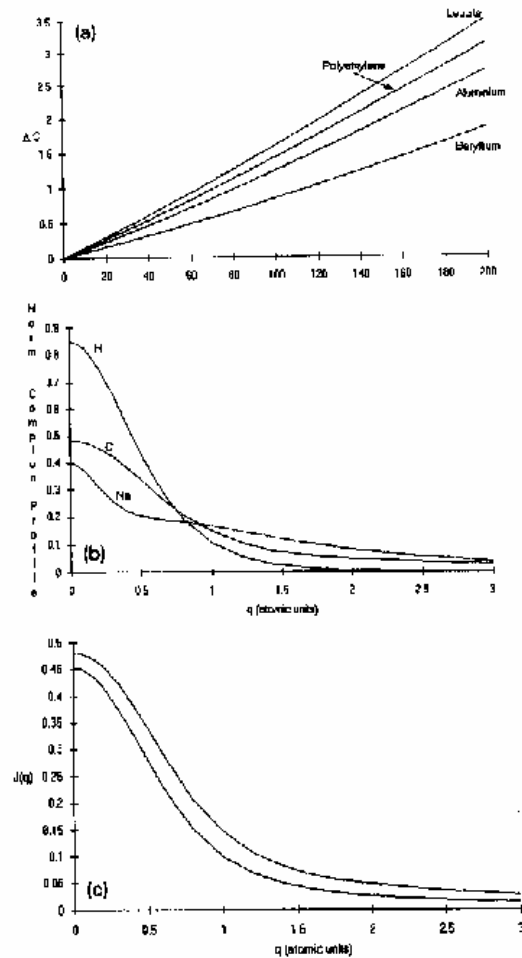
peak. Compton profiles have been calculated by the authors for atomic hydrogen, carbon and sodium (fig. 19b). They show large differences in the shapes of the Compton profiles which is the basis of the analysis. As is shown in fig. 19c, the Compton profile is sensitive to the state of valence electrons, so, different molecules will exhibit different profiles.

(c) *Multiple interactions*. In multiple interactions we can describe the distinction between (i) the multiple-scattering events in which a scattering event is followed by another scattering event, (ii) multiple photoelectric interactions, and (iii) mixed scattering and photoelectric interactions. Multiple interactions enhance the intensity of the whole spectrum, i.e., of its fluorescent and scattered portions. Unfortunately, the analytical treatment of the contribution of multiple interactions is not possible in general due the complexity of the problem. Anyway, some statements can be assumed to be true in general. The probability of a multiple interaction depends on the terms of the absorption coefficient of the sample matrix and on the size of the interaction volume. In particular, the multiple-interaction contributions to the spectrum can be considered negligible when the absorption and self-absorption (of characteristic radiation) are small. Therefore, if the thin-sample approximation holds, the multiple-interaction contribution can be neglected.

In fact, the probability of a multiple interaction depends on the number of photons that are generated in a sample by interactions producing secondary photons. In this case multiple interaction and self-absorption are interconnected, but they produce opposite effects on the spectrum. To give an example, we can consider the case of multiple PE in an alloy. In this case, the problem can be analytically solved [60, 61] and an approximate relation was calculated for enhancement effects from secondary and tertiary photoelectric interactions. The results obtained show that the effect is in general negligible, except in alloys of two or more elements with a highly absorbing matrix: as in the case of iron and copper alloys.

The multiple-scattering contribution to the intensity and energy distribution of the Compton spectrum is an even more difficult problem. In this case, we should take into account not only the total amount of the multiple events, but also the energy distribution of the multiply scattered photons. Some attempts to solve the problem analytically have been made, which can be found in the literature [62, 63], but must be considered to be very crude approximations, partly because they do not include an energy distribution. Multiple scattering can be evaluated with the Monte Carlo method. But these methods are time consuming and give results that in many cases are difficult to extrapolate to the context from which they were obtained. Many interesting results of Monte Carlo calculations have been reported, especially by the groups interested in the development of new devices for the measurement of the Compton profile [64, 65]. The results reported show that the energy distribution of the multiply scattered photons is quite flat and that the contribution can be considered negligible when a light matrix and a small sample have been used. The contribution increases strongly with the size of the sample and the absorption coefficient.

2.2. X-ray fluorescence analysis

This section is based on ref. [66]. As mentioned in section 2, when a sample is irradiated with X-rays of proper energy and intensity, secondary characteristic X-rays are emitted by the sample. The characteristic energies of these X-rays allow for the identification of elements in the sample. The intensity values are in some way proportional to the elemental concentration. In the X-ray spectrum are also present X-rays elastically and inelastically scattered by the sample. In particular, we will consider the following: incident monoenergetic radiation entering the sample normal to the surface and emitted radiation composed of elastically scattered X-rays, Compton-scattered X-rays and characteristic X-rays, also leaving the specimen normal to the surface (fig. 20).

The fluorescent flux from an element a in a layer of mass per unit area $\rho \Delta x$ (g/cm^2) at a depth
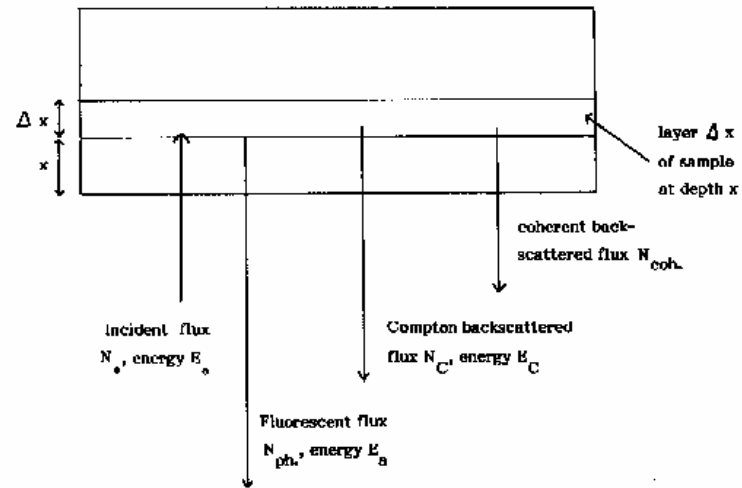

Fig. 20. Physical model for X-ray fluorescence analysis.

ρx (g/cm^2) is

$$\Delta N_a = N_0 K \omega_a \mu_a(E_0)(1 - 1/J_a)c_a \rho \, \Delta x \exp[-\mu_t(E_0)\rho x] \exp[-\mu_t(E_a)\rho x] .$$

where the parameters of the above equation have the significance and the dimensions listed in table 1. Integrating for a specimen of mass per unit area, $m = \rho x$ (g/cm^2),

$$N_a = \frac{N_0 K \omega_a \mu_{ph\,a}(E_0)(1 - 1/J_a)c_a}{\mu_t(E_0) + \mu_t(E_a)} (1 - \exp\{-[\mu_t(E_0) + \mu_t(E_a)]m\}) . \tag{26a}$$

Table 1
List of parameters employed in sections 2.1, 2.2 and 2.3

N_a (photons/cm^2 s)	Fluorescent photon flux density (number of photons per unit area and time) of X-rays of element a.
N_0 (photons/cm^2 s)	Incident photon flux density.
K	Geometrical factor.
ω_a	Fluorescent yield of element a in the shell of interest.
$1 - 1/J_a$	Branching factor which corresponds to the intensity of X-rays in the line of interest over the total X-ray intensity.
c_a (%)	Concentration (% by weight) of element a.
m (g/cm^2)	Mass per unit area of the sample.
ρ (g/cm^3)	Density of the sample.
$\mu_t(E)$ (cm^2/g)	Total mass absorption coefficient of the sample at energy E.
$\mu_{ph\,a}(E_0)$ (cm^2/g)	Photoelectric absorption coefficient of element a at incident energy E_0.
μ_{coh} (cm^2/g)	Absorption coefficient of the sample for coherent scattering.
μ_C (cm^2/g)	Absorption coefficient of the sample for incoherent scattering.

The corresponding equation for the coherent scattered radiation is

$$N_{coh.} = [N_0 K \mu_{coh.}/2\mu_t(E_0)]\{1 - \exp[-2\mu_t(E_0)m]\} .$$ (27a)

The incoherent back-scattered flux is

$$N_C = \frac{N_0 K \mu_C}{\mu_t(E_0) + \mu_t(E_C)} \; (1 - \exp\{-[\mu_t(E_0) + \mu_t(E_C)]m\}) .$$ (28a)

It is very useful to consider two extreme cases for the sample thickness.

2.2.1. Infinitely thick samples

This is the most general case, when liquids, alloys, minerals and so on are analyzed, with a thickness larger than a few tenths of a mm. For infinitely thick samples, the thickness of the sample is larger than the range for the secondary radiation. The following equation should be satisfied:

$$[\mu_t(E_0) + \mu_t(E_a)]m \gg 1 .$$ (29)

In this hypothesis, eqs. (26a), (27a) and (28a) can be written in the form

$$N_a = \frac{N_0 K \omega_a \mu_{ph. a}(E_0)(1 - 1/J_a)c_a}{\mu_t(E_0) + (\mu_t(E_a)} ,$$ (26b)

$$N_{coh.} = N_0 K \mu_{coh.}/2\mu_t(E_0) ,$$ (27b)

$$N_C = N_0 K \mu_C/[\mu_t(E_0) + \mu_t(E_C)] .$$ (28b)

In the approximation $E_C \approx E_0$, the total flux of scattered radiation is given by

$$N_{sc} = N_0 K \mu_{sc}/2\mu_t(E_0)$$ (30a)

when $\mu_{sc} = \mu_{coh.} + \mu_C$.

2.2.2. Infinitely thin samples

A thin sample is obtained, for example, by depositing and drying liquids on thin filters, by vacuum deposition, by applying paints, thin sections of biological tissues and so on. For infinitely thin samples, the attenuation of incident and emitted radiation should be negligible. Therefore, the following condition should be satisfied:

$$[\mu_t(E_0) + \mu_t(E_a)]m \ll 1 .$$ (31)

In this hypothesis, eqs. (26a), (27a) and (28a) can be written in the form

$$N_a = N_0 K \omega_a \mu_{ph. a}(E_0)(1 - 1/J_a)m_a , \quad m_a - mc_a ,$$ (26c)

$$N_{coh.} = N_0 K \mu_{coh.} ,$$ (27c)

$$N_C = N_0 K \mu_C ,$$ (28c)

$$N_{sc} = N_0 K \mu_{sc} .$$ (30b)

Equations (26c), (27c) and (28c) for back-scattered radiation (detector at 180° with respect to the incident radiation) are based on the hypothesis of the isotropic angular distribution. This hypothesis is true for fluorescent radiation, because the photoelectric effect is isotropic, but, as pointed out above, is not correct for scattered radiation, either coherent, or incoherent. The differential cross section for coherent scattering is peaked forward, and this trend increases with increasing incident energy. There is, in general, a minimum value for coherent scattering at 180°. Quite the contrary holds for the Compton-scattered radiation, which has a strong minimum in the forward direction and a relative maximum at 180°. It is therefore very important to calculate the contribution of scattered radiation as a function of angle and incident energy (figs. 4–10).

By considering in eq. (26a) the self-absorption term C,

$$C = \frac{1 - \exp\{-[\mu_t(E_0) + \mu_t(E_a)]m\}}{[\mu_t(E_0) + \mu_t(E_a)]m} ,$$ (32)

eq. (26a) can be written as

$$N_a - N_0 K \omega_a \mu_{ph. a}(E_0)(1 - 1/J_a)c_a mC .$$

The variation of the self-absorption term C versus the thickness of the sample is shown in fig. 21 for water, copper and lead. When $C - 1$, the thin-sample condition is satisfied. From eq. (26b) one can deduce:

– In the limit of infinitely thin samples, there is a linear relationship between fluorescence flux N_a and concentration c_a of element a. No interelement effects occur.

– The fluorescence flux from a thin sample is about an order of magnitude less than from a thick one, but the fluorescence to scatter ratio is several orders of magnitude larger. Because the minimum detection limit is strongly influenced by the flux of scattered radiation, much better MDL values can be obtained by analyzing thin samples.

– For thick samples there is no advantage in increasing the incident flux beyond about 10^7 photons/s, because of the larger amount of scattered radiation and the inability of the electronics to process more than about 10^4 counts/s without strong energy-resolution losses.

2.2.3. Minimum detection limit

Following the derivations of Currie [67], a useful definition for the minimum detectable limit (MDL) based on Poisson counting statistics for 95% confidence in detection is

$$MDL = (3.29/S)\sqrt{R_b/t} ,$$ (33)

where R_b is the background area under the X-ray peak of interest, S the sensitivity of the instrument for that specific element expressed as counts per $\mu g/cm^2$ of concentration and t the measuring time. To obtain the smallest MDL, the flux of the exciting X-rays, N_0, should be as large as possible, however limited to the number of photons which can be processed by the detector and the electronics. Also the
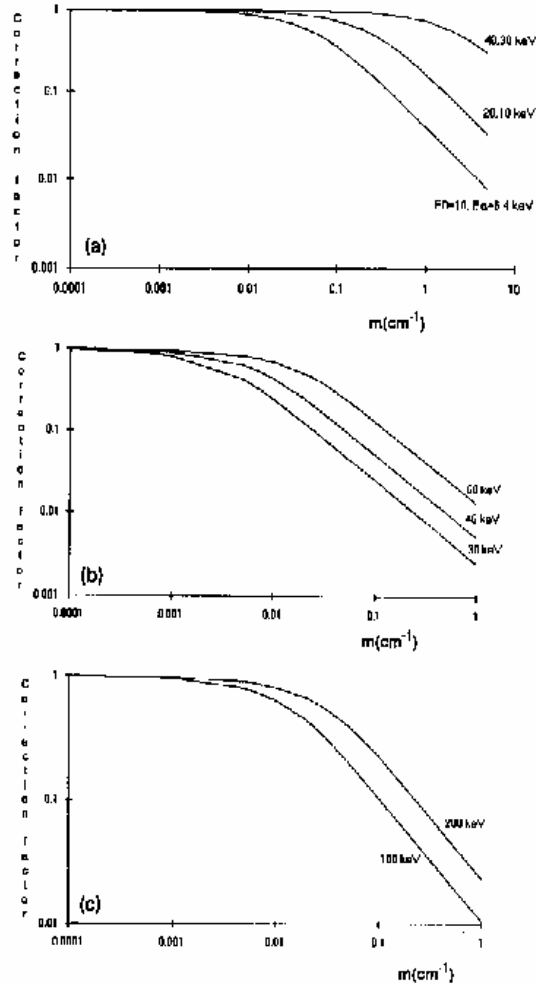
Fig. 21. Matrix correction term C versus thickness m (cm) of water, for E_0 10, 20 and 40 keV (E_4 6.4, 10 and 30 keV) (upper curves), of silver for E_0 100 (E_4 = 30, 40, 60 keV) (middle curve) and for lead for E_0 200 (E_4 100 keV).

photoelectric absorption coefficient for the production of characteristic X-rays, $\mu_{ph,a}$ should be maximized. However, the largest value of $\mu_{ph,a}$ does not necessarily correspond to the energy which produces the smallest MDL value [68].

This can be done by selecting an optimal value of incident energy, close to the photoelectric edge of

the element to be analyzed. For that reason, monoenergetic radiation of variable energy is preferable for XRF-analysis, instead of bremsstrahlung radiation. Further, to obtain the smallest MDL, the background counts R_b should be considered. Assuming that the background counts under the photoelectric peaks are mainly due to scattered radiation, these are proportional to the term $(m\mu_{sc})$ (mass per unit area of the sample and of the support, multiplied by the absorption coefficient for scattering processes). It is therefore important to reduce if possible the mass of the sample. For example, the matrix mass can be reduced by ashing, by filtering a liquid sample through filters and so on, and/or by reducing the support of the sample.

2.2.4. Polarized X-ray sources

The bulk of the background observed in photon excitation is proportional to the intensity N_0 of the primary beam scattered by the sample [see eqs. (30a) and (30b)]. One method of reducing this intensity takes advantage of the fact that the scattering is minimum in the direction of the electric vector of the incident electromagnetic radiation (figs. 2). Most sources of photons, for example radioactive sources or X-ray tubes produce unpolarized photons. However, it is possible, by successive scattering of an unpolarized beam, to polarize it. By placing the detector in the plane of polarization, it is possible to minimize the intensity of the scattered radiation without decreasing the fluorescent counts, because the photoelectric effect is insensitive to polarization. The reduction in background for a beam which is partially polarized by successive scattering has been demonstrated by several workers [69, 70]. The limitations on the use of this technique is the inherent and strong loss of intensity through the multiple-scattering processes.

As an example, background for polarized [241]Am radiation and for direct [241]Am radiation is shown in fig. 22 [69]. One method of obtaining intense polarized beams is to use the radiation emitted by very high-energy electron storage rings (synchrotron radiation) (see for example ref. [70]). Synchrotron radiation is nearly linearly polarized with the electric vector in the plane of the electron orbit. It is highly directional and can give rise to useful intensity, as high as 80–100 keV. The high degree of polarization can be maintained while focusing the flux on the sample. Polarized radiation was recently
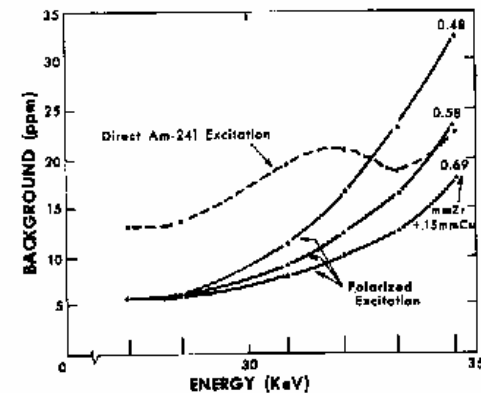

Fig. 22. Background in the energy interval 27–35 keV for polarized radiation (with three filter thicknesses) and for Am241 excitation in the same detector from Kaufman [69].

employed for "in vivo" analysis of medium and heavy elements in the human body [71, 72]. In these cases the sensitivity for analysis is very good, of the order of μg/g. In the case of "in vivo" analysis of medium and heavy elements, the combination of incident energy and scattering angle results in a background dominated by Compton scattering [73].

Referring back to eq. (7) for the Klein–Nishina differential cross section, α is the angle between the directions of the electric field vectors of the incident and scattered photon; then an equivalent expression is

$$d\Omega/d\sigma = \tfrac{1}{2}r_0^2(K/K_0)^2(K/K_0 + K_0/K - 2\sin^2\theta\cos^2\alpha) ,\qquad(34)$$

where θ is the scattering angle and α is the angle between the planes of polarization of the incident photons and scattered photons. This illustrates that polarized incident X-rays can be used to reduce scattering. For example, Christofferson and Mattsson [71] and Jonson and Unsgaard [72] have analyzed cadmium in the kidney cortex of a man and platinum in the right kidney of a man by using partially plane-polarized photons. In the latter case, the photons are polarized by scattering the primary X-rays (155 kV, 25 mA) in three mutually orthogonal directions before they reach the detector, since the scattering of plane-polarized X-rays will be minimum into 90° in the plane of polarization of the secondary beam (fig. 23). The effect of polarization on the spectrum is shown in fig. 24.

2.3. Scattering techniques

The study of scattering events has long been a source of information in the physical sciences, and for example X-ray scattering was recognized as a problem in image formation from the beginnings of radiology. Coherent scattering has a great probability to occur at very low photon energies and angles in materials with high atomic number; whereas Compton scattering may occur at higher energies in
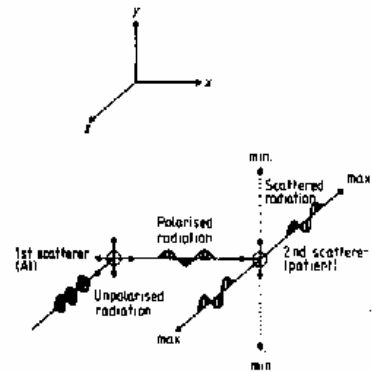
Fig. 23. Beam geometry to obtain polarized X-rays. By scattering the primary X-ray beam in two mutually orthogonal directions the fluence rate of incoherently scattered X-rays is shown in the Z direction (from Jonson [72]).
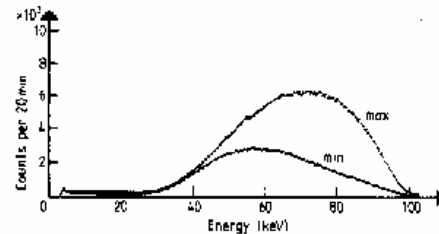
Fig. 24. Pulse height distribution when photons are collected in the direction of minimal and maximal scattering (from Jonson [72]).

materials with low atomic number. Therefore there is a large degree of complementarity in the information that we can obtain; this fact is largely exploited by the scattering techniques.

Several analytical methods have been proposed using only Compton-scattered radiation (or scattered and transmitted radiation) to assess the electron density within a particular internal part of an object. Applications of these methods have been reported in three main areas: (a) densitometry [62–64, 73–77]; (b) whole-body tomographic imaging [78–80]; (c) material analysis. These techniques can be subdivided into four groups: (i) dual- and single-energy Compton-scattering densitometry [63, 73, 75]; (ii) mass determination [81]; (c) Compton-scattering imaging [75–85]; and (d) Compton profile measurements [35, 44].

It is worth noting that the most frequent use of Compton-scattered radiation is in relation to the energy-dispersive X-ray fluorescence techniques (XRF). In this case, the Compton peak is used in normalization procedures in order to correct for (i) measuring time, (ii) self-absorption, and (iii) sample mass. The last application is very useful when we must examine samples of variable mass and thickness as environmental samples, thin solid layers (films) and biological thin sections. The correction method is based on the relationship existing between the intensity of the Compton-scattered radiation and the sample mass involved in the scattering processes [see for example eq. (53)] [81]. Obviously, the Compton-scatter intensity is also a function of the sample composition; this limitation is very strong in samples of variable composition (at small values of momentum transfer) especially for high-Z materials.

More recently, also low-angle X-ray scattering has become an important area of research since it represents the unfolding of further diagnostic information from transmission imaging procedures. A CT-imaging system utilizing small-angle scattering was for example described by Harding et al. [119].

2.3.1. Techniques using the transmitted and Compton-scattered photons

In the early seventies two different Canadian groups described the basic method for Compton densitometry, using transmitted radiation to correct the attenuation effects [63, 73]. In this method a single- or dual-energy configuration may be used according to the primary photon energies and scattering angle. The simple idea on which these methods are based is that of calculating the attenuation of the primary and scattered beam, through transmission measurements, using sources of appropriate energy. In particular, the Compton-scattered photons, in a given direction, display an energy distribution around a value that can be calculated by eq. (23). Therefore, by using a second source having this energy one can correct for the attenuation of the Compton-scattered beam. A certain number of matched pairs of low-energy monoenergetic γ-sources may be proposed for this type of measurement, the only limitation being, in practice, the number of available radioisotope emitting photons in the range 80–130 keV [75], this being the optimal range for the energy primary radiation [69].

Figure 25 is the basis to better understand the method. The basic strategy is to perform two scatter measurements rotating the sample through an angle of 180° and, simultaneously, two transmission measurements, using a second detector. It is essential to pass through the same beam paths, during the transmission and scattered measurements. These four measurements allow us to calculate the attenuation factors of the beam reaching the sample placed near the center of the object. In this method, the sample should have a very small size.

The electron density is proportional to the ratio of the scattered to the transmitted intensities. Therefore, this method can be used to determine the electron density of the sample, but not its mass density. The latter can be deduced knowing the value of the effective Z/A ratio (see below) of the sample under study. It is worth noting that, at the energies and scattering angles used in these
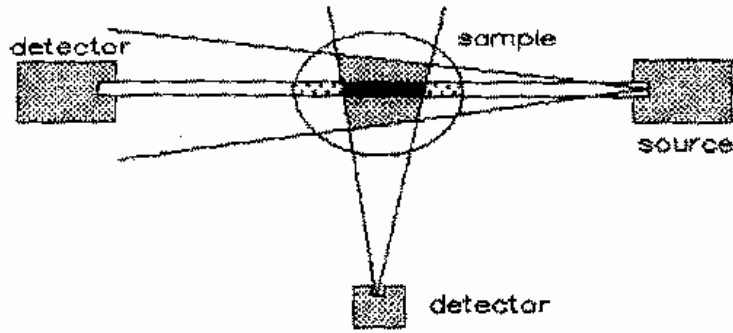
Fig. 25. Basic principles of Compton-scatter densitometry.

Compton-scattering techniques, only a proportionality relation exists between the electron density and Compton-scatter intensity. For low-Z materials, the proportionality constant can be determined by performing the set of measurements on a water sample. Using this procedure we cannot completely correct for the difference in elemental composition of the standard sample, water, and the unknown sample. Another inherent limitation is that the path length of the transmitted and scattered radiation in the object should be the same. As is shown in fig. 25, the dimension of the transmitted photon beam is determined solely by the detector collimation, while the shape of the scattered photon beam is defined by the combination of both source and detector collimators.

The assumption that the sample size is very small implies that self-absorption effects can be neglected. Good results are thus obtained only for small variations of the sample size. Huddleston and Bhaduri [74] have shown that measurements with this photon scattering technique are strongly dependent on the sample size. They have attributed the observed bias, in the electron density determination, to the concomitant action of the multiple scattering and the self-absorption effects.

Many changes in the original method have been proposed by various authors. Olkkonen and Karjalainen [75] in particular described a single-source, low-energy, small scattering-angle method; this method has later been extensively used by Huddleston and coworkers [74, 76]. In addition, Webber and Coates [77] have constructed a three-source densitometer for the measurement of lung density. This system avoids the necessity of rotating the object. Cooper et al. [82] have developed a single-source densitometer using a Cs137 gamma source and a scintillator for industrial uses. With this system they have obtained excellent results in the densitometric measurements of low-density liquids in high-density casings, e.g., liquids in pipes and voids, inclusions and segregation impurities in transition-metal alloys.

Garnett et al. [73] have demonstrated that for the measurement of bone density with Compton scattering the analysis is optimized when the photon energy is about 90 keV. To reach this conclusion they considered (a) the Compton-scattering differential mass-absorption coefficient; (b) the total mass-absorption coefficient of soft tissue and bone; (c) the detector efficiency; and (d) the time required for a given dose from a fixed source strength. For materials with higher Z optimal energy range will shift towards higher energies. The analytical performance of photon scattering techniques both in laboratory and "in vivo" measurements are well established. In the assessment of bone density, Webber and Kennett [62] have found that with three-minute measuring time it is possible to obtain a statistical

precision of 1% with an overall precision of 1.5%. They studied the accuracy of the technique in relation to the major sources of error, i.e., finite geometry, non-identical geometry and multiple scattering. After a careful study, they found that the measurements usually underestimate the electron density and that the accuracy is 10%. Finally, Huddleston and coworkers [74, 76] observed that the density was overestimated for higher densities and for larger samples. These authors showed that corrections can be made using linear approximations [74]. Shrimpton [83] studied the analytical performance of this method in the determination of the electron density of different low-Z liquids. Using laboratory equipment and performing measurements on thirteen different liquids, it was demonstrated that a very good linear correlation can be achieved between measured and theoretical electron-density values (fig. 26). This result clearly reveals the analytical capabilities of this method.

One of the most promising uses of this method is the "in vivo" determination of lung density, because of the wide range of densities (0.26–1.06 g/cm³). These variations in density are only due, in part, to the state of the lung. Further, Webber and Coates [77, 84], using a three-source densitometer optimized for this application, have shown good results in terms of statistical precision (2.2%), total precision (~5%) and accuracy. More recently, Huddleston and Weaver [76] have introduced a new Compton-scatter method using a dichromatic source. This method has the advantage of avoiding the rotation of detectors and sources around the sample under examination. A schematic drawing describing the dual-energy Compton-scatter method is shown in fig. 27. This method assumes that the measuring system in use has a smaller scattering volume compared to the sample size. Now, if we study the Compton-scatter intensity produced in samples of increasing size, we would note that the scattered intensity decreases with increasing sample size. This phenomenon is due to the absorption of the
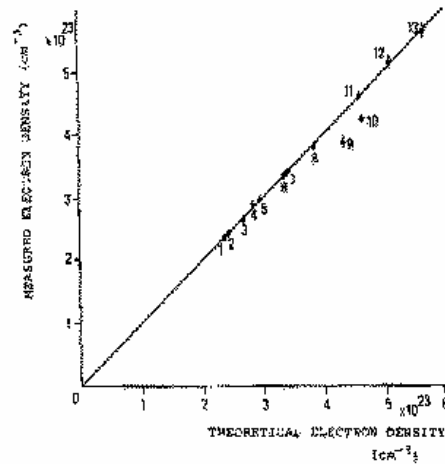
Fig. 26. Comparative plot of measured versus calculated electron density for the following liquid samples: 1. n-heptane; 2. diethyl ether; 3. isopropyl alcohol; 4. xylene; 5. ethyl acetate; 6. water; 7. glacial acetic acid; 8. formic acid; 9. chloroform; 10. carbon tetrachloride; 11. fuming nitric acid; 12. perchloric acid; 13. concentrated sulphuric acid (from Shrimpton [83]).

Fig. 27. Schematic drawing of the geometry of the source-detector system in dual-energy Compton densitometry.

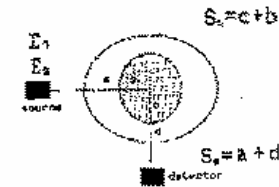primary and scattered photons by the sample parts not under investigation in the scattering processes. Therefore, if we assume that the scatter intensity decreases exponentially with increasing path lengths of the two beams in the sample, we can deduce the electron density knowing the path lengths of the beams in the sample. The absorption coefficients are assumed to be known or have been estimated independently. From the few results published so far, the characteristics of this method seem to be very interesting. In fact, Huddleston and Weaver [76] have shown that an accuracy of 3.5% can be reached. The big advantage of this new method is in the possibility of using high-energy photons. This reduces the influence of some major sources of error, such as multiple scattering, finite geometry and attenuation.

Recently, Loo et al. [32] developed a new Compton densitometer in which a HpGe detector is used in order to measure the spectral distribution of the incoherently scattered photons. They showed, with an empirical approach, that it is possible to evaluate density gradients in a sample with only one measurement. This method is very similar to that previously proposed by Farmer and Collins [85], but the results they have obtained are of better quality, due to a careful optimization of the spectrometer design.

2.3.2. Compton-profile measurements

The Compton profile has been considered an extraordinary source of information by some scientists interested in the modifications of the electron momentum distributions in the sample [35, 44]. Unfortunately, the difficulties in performing "profile" measurements have limited the use of this technique. The possibility to use the measurement of Compton profile as an analytical tool in applications has been considered in the last decade by few authors [30, 59]. In fact, a precise measure of the Compton profile in a finite sample is difficult, due to the presence of the attenuation and multiple scattering. Many authors have studied the spectral distribution of the multiply scattered photons showing the important influence of the sample dimensions on the spectra [86, 87]. Some measurements performed by two of us [88] have led to the conclusion that the geometrical effects are also a severe limitation for this kind of measurements. Methods for theoretically determining geometrical effects have been recently developed [89]. So far, few experimental results of analytical applications of the Compton-profile measurement have been published. The only possibility that we can conceive of is the development of high-flux, high-brilliance monochromatic sources of more than 50 keV, with which to perform measurements of the Compton profile in a finite sample using very narrow-collimation and position-sensitive detectors.

2.3.3. The coherent (Rayleigh) to Compton scatter ratio

Both coherent- and Compton-scattered photons are collected by a detector within the same solid angle. The ratio R/C is therefore independent of the geometry. The ratio of the coherently to Compton-scattered photons is given, under the usual assumptions regarding multiple scattering and other higher order processes, by

$$R = \frac{N_{coh}}{N_C} = \frac{F^2}{S} f(E_0, \theta) , \quad f(E_0, \theta) = \frac{(d\sigma/d\Omega)_{Th}}{(d\sigma/d\Omega)_{KN}} ,$$ (35)

where $f(E_0, \theta)$ is the ratio of the Thomson to the Klein–Nishina cross sections [see eqs. (4) and (7)]. It is independent of the atomic number. The terms F (atomic form factor) and S (incoherent scattering function) have been defined previously in eqs. (12) and (15).

The R/C ratio at various scattering angles, incident (monoenergetic) energies and scattering materials, is shown in figs. 28–32. It is important to note that to resolve, in many cases, the coherent peak from the Compton peak, a detector with good energy resolution is required. The availability of solid state detectors with high energy resolution and high counting efficiency, improved, therefore, significantly the study of the R/C ratio. The first proposal to use the ratio of the two scattered peak intensities was made by Kunzendorf in 1972 [90]. This work immediately showed the potential of the method, despite the primitive (uncollimated) set-up used in the measurements. The Kunzendorf results were obtained with a back-scattering geometry, using a Si(Li) detector (FWHM 250 eV) and radioisotopic sources of plutonium 238 (emitting 13.5, 17.2 and 20.2 keV photons), cadmium 109 (22.1
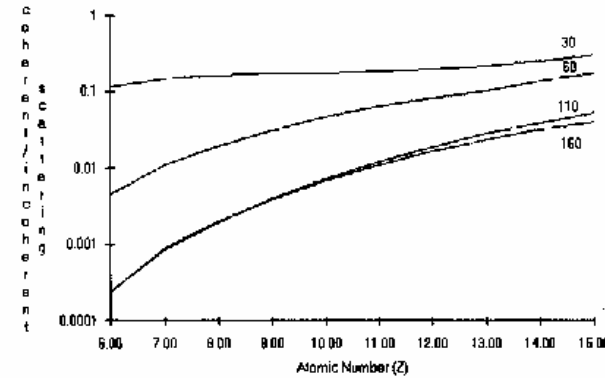

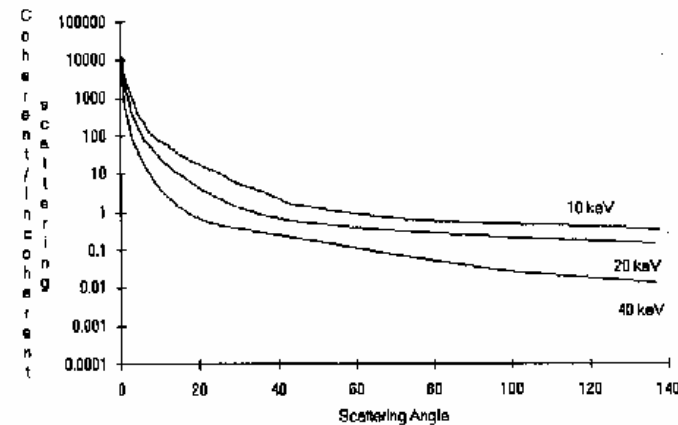Fig. 28. R/C ratio for biological materials (Z = 6–12) at 30°, 60°, 110° and 150° for E₀ - 59.6 keV.

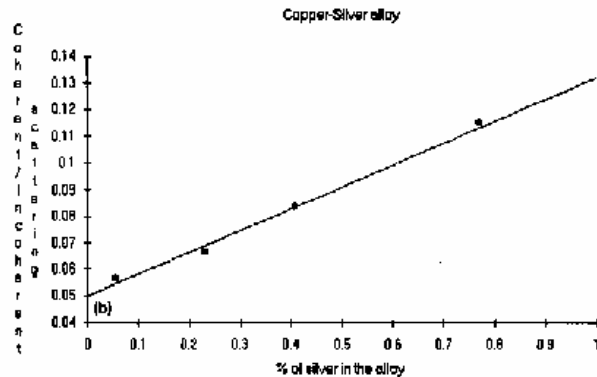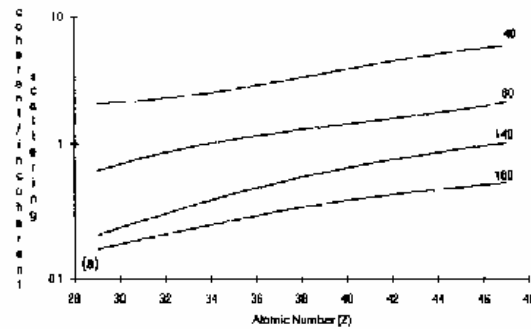Fig. 29. R/C ratio for water at 10, 20 and 40 keV versus scattering angle.

Fig. 31. R/C ratio for heavy elements ($Z = 78–82$) at $E_0 = 100$ keV, for scattering angles of $30°$, $60°$, $110°$ and $150°$.

Fig. 30. R/C ratio for intermediate elements ($Z = 29–47$) at $40°$, $60°$, $140°$ and $180°$ for $E_0 = 40$ keV (a); R/C ratio for Cu–Ag alloys (b, at 59.6 keV). Theoretical values (——) and experimental values (·) are compared.

and 24.9 keV) and americium 241 (59.4 keV). The reported results demonstrated that the value of the power index of the R ratio versus Z, was greater for higher energies of primary photons. Later, a Finnish group started extensive studies on this method; they proposed the use of the R/C ratio in the measurement of trabecular bone mineral determination (TBMD) using an americium-241 source and a ninety-degree scattering angle [91].

Schatzler [92], in 1979 described the first analytical applications of the R/C method, using an americium 241 source and scattering angles of 48° and 68°. Using twenty-six organic compounds, he found a relationship between the R/C ratios and the effective atomic number. His aim was to demonstrate that it is possible to identify a compound only by measuring its R/C ratio; fig. 33 shows the plot of the R/C ratios, relative to water, as a function of the effective atomic number. Schatzler approximated these values with a power function obtaining an index of 3.5, which agrees with the strong dependence of the coherent-scattering coefficient on Z. Schatzler also gives examples of the
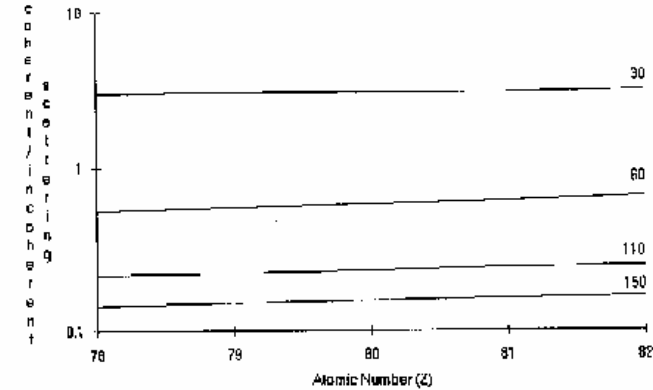
analysis of binary mixtures; he attempted to determine the percentage of fat content in milk and meat [92]. From the results reported it can be seen that a precision of 3–4% can be reached with a measuring time of a few hundred seconds.

Similar results have been obtained by Puumalainen et al. [93] in the determination of iodine in tissues; in fact, the results reported, showed a sensitivity of about one milligram per cubic centimeter. It can be observed that the typical sensitivity of the R/C technique, in the measurement of the concentration of a particular element in a sample is very low if compared with that of other analytical techniques such as X-ray fluorescence and activation analysis. However, these techniques can be used for "in vivo" measurements. The above-mentioned results, characterized, already in the very early attempts, the R/C method as an analytical technique with which to perform bulk analysis rather than the determination of a single trace element.

Almost simultaneously in 1980, some groups again proposed the use of the R/C technique for the determination of TBMD, using a small scattering angle and energies around one hundred keV [94, 95]. In particular, Stalp and Mazess [95] carried out experimental studies on the behavior of the R/C ratio using radioisotopic sources of americium 241 and gadolinium 153 and a scattering angle of less than sixty degrees. Their conclusions were that with a 103 keV energy of the primary beam and a $30°$ scattering angle (i.e., at a value of momentum transfer of $q = 2.15$), better results can be obtained than with an americium 241 source scattered into $90°$ ($q = 3.42$). Stalp's conclusions can be explained considering that, at 103 keV with a scattering angle of $30°$, there is, at the same time, a lower q value and a lower attenuation of the primary beam and scattered radiation. However, it should be pointed out that, in that work, the authors did not attempt to optimize the geometry at different angles using the same collimation condition at $30°$ and $60°$. No larger scattering angle was investigated.

For a low-Z matrix, Kerr et al. [94] discussed a procedure to optimize the performance of the measuring system, with respect to the primary beam energy and scattering angle. Using this procedure, they found that, with their very tightly collimated experimental set-up, the best conditions would be at an energy of 80 keV and a scattering angle of $25°$. The procedure was as follows: for a given energy and scattering angle, the FWHM of the Compton band was determined by assuming a certain range of
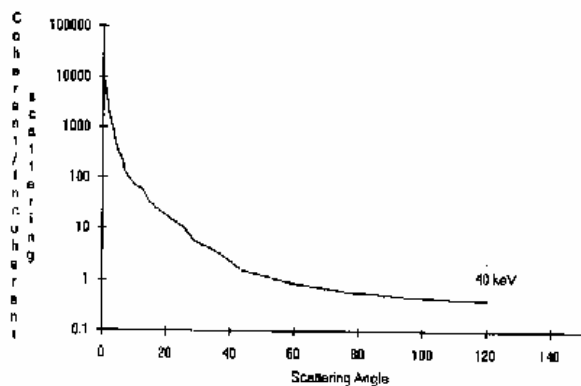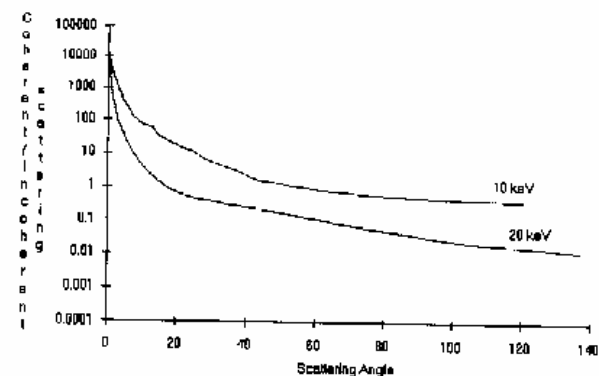
Fig. 32. R/C ratio for water, copper and silver versus scattering angle θ.

Fig. 33. The coherent to Compton scattering ratio, relative to water, for 26 organic compounds. The primary beam energy was $E_0 = 49.6$ keV and the scattering angle $\theta = 68°$ (from Schatzler [97]).

Fig. 34. Scattered spectrum from a cadaver foot. Incident energy $E_0 = 103.2$ keV, scattering angle $\theta = 22.5°$ (from Kerr et al. [94]).

Fig. 35. The energy dependence of the performance of a system for the measurement of trabecular bone mineral density based on the R/C method. A, number of coherently scattered photons per unit time, B, detector counting efficiency, C, mass absorption coefficient for bone, D, overall performance (from Kerr et al. [94]).

scattering angles along with the detector resolution. The coherent peaks and the Compton band are considered to be resolved when the upper limit of the full-width at tenth maximum FWTM of the Compton band coincides with the lower limit of the FWTM of the elastic peak. Having determined the minimum acceptable coherent-Compton separation in this way, the corresponding Compton energy shift was then calculated. With this procedure it is possible to find, for a given energy (and known values of the collimation parameters), the minimum scattering angle that can be usefully employed. Figure 34 shows the spectrum of photons scattered from a foot using a primary beam energy of 103 keV and a scattering angle of 22.5°. To find the optimal range of primary photon energies the authors studied the energy dependence of: (i) the number of coherently scattered photons per unit dose, (ii) the detector (an intrinsic planar germanium 400 mm² active area counting efficiency), (III) the differential coherent-scatter mass-absorption coefficient. Figure 35 shows the plot of these functions [94]. It is evident that an energy around 80 keV is the most favourable.

In 1982, Ling et al. [96], published the results, in the measurement of TBMD, using americium 241 sources and larger scattering angles. They discussed the experimental obstacles encountered in the development of a measuring system for clinical use. They showed the advantages of using a 90° angle geometry in order to obtain a scattering volume of a more regular shape compared to the elongated form obtained at smaller and larger angles. These authors, depicted the methodology for studying the different sources of error in an "in vivo" system. In two later papers [97, 98], the authors pointed out

that the best sensitivities can be obtained either at larger scattering angle, for a 60 keV primary beam energy, or, which is equivalent, at higher momentum-transfer values. In particular, they showed that the figure to optimize is the precision in which the counting rate and the sensitivity are simultaneously considered. Their conclusions were that the optimizing procedure proposed by Kerr et al. [94] must be completed by taking into account the changes in sensitivity and precision observed at higher momentum-transfer values.

Finally, these authors clearly pointed out the importance of the geometrical counting efficiency that changes considerably at different scattering angles. So far this group is the only one to have published results on the clinical use of the R/C technique in the measurement of TBMD [99]. Using a 70° angle and a 1.2 Ci americium 241 source, they obtained an accuracy of 5% and a precision of 3% with a counting time of 15 minutes. The dose to the patient is about 300 mRad. Figure 36 shows a comparison between bone mineral density determined by the R/C technique and measured directly. Gigante and Sciuti [100, 101] completed the analysis of the above mentioned group [97, 98] showing that a back-scattering geometry can be used to optimize the performance of the system in measurements in peripheral bone sites. Studies on the shape of the scattering and the behavior of the self-absorption function in a back-scattering geometry were also carried out. An interesting development from the instrumentation point of view was illustrated by Puumalainen et al. [102] with the use of an X-ray tube in the place of the less intense radioisotopic sources. The aim of these authors was to obtain a more intense primary beam, possible with a tunable energy. The monochromatic beam was obtained using a CsCl filter, and a tube voltage of 59 KV. They thus obtained a 38.9 keV energy beam, useful only for "in vitro" studies.

Later, the Cooper group [103, 104] studied the possibility of obtaining higher energy monochromatic radiation from an X-ray tube by filtering the primary beam and the scattered radiation with rare-earth foils. In this way, it is possible to use a scintillation detector opening the possibility to use the ratio technique in an industrial environment. The availability of more intense X-ray sources, such as synchrotron radiation, may give a new impulse to these techniques.
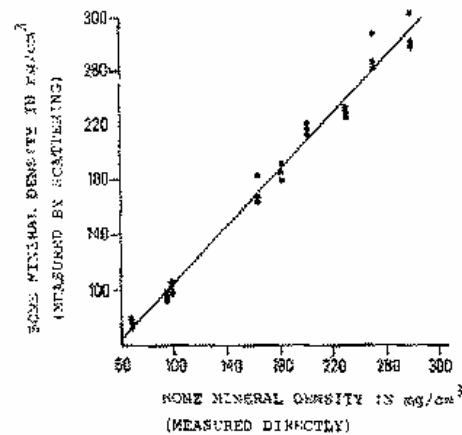

Fig. 36. Bone mineral density determined by the R/C method and that measured directly (from Greenfield et al. [99]).

Besides the very interesting application in the determination of TBMD, R/C techniques have other analytical applications in the identification of unknown materials and/or in the characterization of tissues. The latter was studied by Holt and Cooper [44], using a spectrometer explicitly set up for Compton-profile analysis [105]. This spectrometer uses a 5 Ci americium 241 source with a scattering angle of 171°. The results demonstrated that accurate characterization of the tissue, through the determination of their R/C ratios, can be obtained. Table 2 shows the R/C values reported in that work, as measured in different tissues and a low-Z sample. Other measurements [105] carried out with saline solution up to 20% have shown that R/C techniques provide a good precision. In fact, a 0.2% change in saline concentration gives a measurable 2.5% change in the intensity ratio. These authors underlined that in order to obtain such good results, a careful study of the Compton profiles is necessary, to minimize the errors in the R/C measurements.

Several investigations have been carried out on the analytical power of R/C techniques, in the identification of low-Z compounds and in the analysis of metal alloys. Gigante and Sciuti [101] have studied the possibility of simultaneously using the scatter and fluorescence information. This is only possible when some elements can be fluoresced emitting photons of sufficiently high energy. In many instances the two pieces of information are complementary and can be simultaneously employed. This strategy is particularly useful in the analysis of tertiary and quaternary alloys, possibly using scatter intensities from the same material at different primary beam energies [106]. Furthermore, authors have shown that identification of low-Z materials is only possible using the R/C ratio. The calculated values of the scatter R/C intensity ratio are compared in fig. 37, with those measured with a spectrometer, using a back-scattering geometry and two americium 241 sources. Gigante and Sciuti [101] have shown that semiautomatic identification of a sample is possible using the theoretical R/C values for the single elements, and a specific computer programme. Corrections for the attenuation effects can be made using the tabulated values of the attenuation coefficients. Bui et al. [107] have studied the capability of this technique for a quantitative analysis of metal alloys.

Manninen et al. [108] first, and later Manninen and Koikkalainen [109] studied the possibility to define an effective atomic number. They carefully studied the behavior of the R/C ratio as a function of Z, both for pure elements and low-Z compounds. They found that good agreement can be obtained between calculated and measured R/C values, for an energy of 60 keV and large scattering angles. Figure 38 shows the results obtained by these authors at different scattering angles. The measured Z values differ from the effective calculated values by less than 0.5%.

The analytical capability of R/C techniques is clearly shown by the results reported above. The

Table 2
Measured R/C ratio of selected samples

Sample	$R/C \times 10^{-2}$
De-ionized water	1.023 ± 0.017
0.9% saline solution	1.210 ± 0.017
Breast cyst fluid	1.163 ± 0.017
In-tissue liver[a]	1.246 ± 0.017
In-tissue liver[b]	1.277 ± 0.017
Homogenised liver[a]	1.180 ± 0.031
Homogenised liver[b]	1.197 ± 0.031

[a] Taken from rats treated with saline solution
[b] Taken from rats treated with phenobarbital (80 mg/kg) solution.

Fig. 37. Measured versus calculated R/C ratio for various compounds (from Gigante and Sciuti [1990]).

Fig. 38. Measured R/C ratio for various compounds, for an incident beam energy of $E_0 = 59.6$ keV and different scattering angles.

sensitivity of this technique is very good for both the determination of the TBMD "in vivo", and the identification of tissues and materials. Further improvements are possible, using more intense monochromatic sources and higher performance detectors. R/C techniques, in the near future, will probably become one of the chosen techniques in tissue characterization and bulk analyses.

3. Imaging techniques

3.1. Physical principles of CT-transmission

Let us consider again eqs. (22a) and (22b) and, in particular, the mass-attenuation coefficient μ/ρ (in cm^2/g). If the absorber is a chemical compound or a mixture, its mass-attenuation coefficient μ/ρ can be approximately evaluated from the coefficient of the constituent elements,

$$\mu/\rho = \sum_i w_i \mu_i/\rho_i , \tag{36}$$

in which w_i is the weight fraction of the ith constituent. The mass-attenuation coefficient is also proportional to the total photon interaction cross section per atom σ_{tot}^a (in $cm^2/atom$). This total is the sum of the cross sections for all elementary processes: photoelectric-effect, atomic Compton scattering, Rayleigh scattering.

The correlation between attenuation coefficient and atomic cross section is

$$\mu/\rho = \sigma_{tot}^a N_a/A , \tag{37}$$

where N_a is the Avogadro number and A the atomic mass of the absorber. Since there are Z electrons per atom,

$$\mu/\rho = \sigma_{tot}^c N_a Z/A = \sigma_{tot}^c . \delta_e , \tag{38}$$

where σ_{tot}^e ($cm^2/electron$) is the total cross section per electron and the expression $N_a Z/A = \delta_e$ represents the number of electrons per gram. For all elements except hydrogen, δ_e approximately equals $\frac{1}{2} N_a \approx 3 \times 10^{23}$ (see table 3). This indicates that the dependence of μ/ρ on the atomic composition is principally related to that of σ_{tot}^e. Considering now the three effects contributing to the attenuation coefficient, we have from eq. (38),

$$\mu = \rho \delta_e (\sigma_{ph}^e + \sigma_C^e + \sigma_{coh}^e) , \tag{39}$$

in which $\rho \delta_e = \rho_e$ is the electron density (electrons/cm^3).

It should also be observed that the Compton cross section σ_C^e (table 4) is independent of the atomic number Z and the contribution of coherent scattering is less than 10% of the total attenuation.

Table 3
Electron density δ_e (number of electrons per gram) versus atomic number

Atomic number	Element	Electron density δ_e ($\times 10^{23}$)	Atomic number	Element	Electron density δ_e ($\times 10^{23}$)
1	H	6	23	V	2.7
2	He	3	26	Fe	2.8
6	C	3	29	Cu	2.75
8	O	3	42	Mo	2.64
13	Al	2.9	50	Sn	2.5
15	P	2.9	53	I	2.5
17	Cl	2.9	82	Pb	2.4
20	Ca	3	92	U	2.3

Table 4
Compton electron cross section σ_e^c versus atomic number at 100 keV

Atomic number	Element	Electron Compton cross section (b/electron)	Atomic number	Element	Electron Compton cross section (b/electron)
1	H	0.494	29	Cu	0.493
6	C	0.495	42	Mo	0.493
13	Al	0.493	50	Sn	0.492
15	P	0.493	53	I	0.492
20	Ca	0.492	82	Pb	0.493
26	Fe	0.492	92	U	0.492

Therefore

$$\mu = \rho \delta_e (A + BZ^{\beta}) \ ; \qquad \beta = 3 \text{--} 4 \ , \quad A, B \text{ constant} \ . \tag{40}$$

In eq. (40) we have explicitly separated the contributions of physical density and atomic number. In the energy region where the Compton effect is predominant, we have

$$\mu = \rho \delta_e A \quad \text{or} \quad \mu \propto \rho \ , \tag{41a, b}$$

and the Compton linear-attenuation coefficient is linearly proportional to the mass bulk density of the absorber (fig. 39). In the low-energy region, where the photoelectric effect is predominant,

$$\mu = \rho \delta_e BZ^{\beta} \ , \quad \mu \propto \rho Z^{\beta} \ , \tag{42}$$

and the linear-attenuation coefficient critically depends on the atomic number of the absorber.

Since tomography is based on many narrow-beam X-ray attenuation measurements, it gives rise to a

map of attenuation coefficients. The characteristics of the image should reflect the dependence of the total attenuation coefficient on the density and atomic number of the absorber. Therefore, CT-images carried out with monoenergetic radiation give information about the atomic number in the photoelectric (low-energy) region and about the physical density in the atomic Compton (high-energy) region (fig. 40).

3.2. Differential tomography

The attenuation coefficient of any element exhibits sharp discontinuities ($K, L, \ldots$) corresponding with the minimum energy values for the ejection of the electron from its shells (see fig. 41). For a quantitative evaluation, values of the attenuation coefficients of Fe, Ag, I and Pb near K- and L-edges are shown in table 5. As can be observed, the difference in the attenuation coefficient above and below the edges is large.

When two attenuation measurements are carried out with a pair of monoenergetic radiation beams, whose energies bracket the P.E. discontinuity of the element, the difference between the two measurements is sensitive only to the presence of the element itself. This effect has been well known for a long time in radiology for the visualization of iodinated vessels (energy-dependent subtraction angiography). In this case, bremsstrahlung radiation was employed generated at different HV-values of the X-ray tube, instead of monoenergetic radiation.
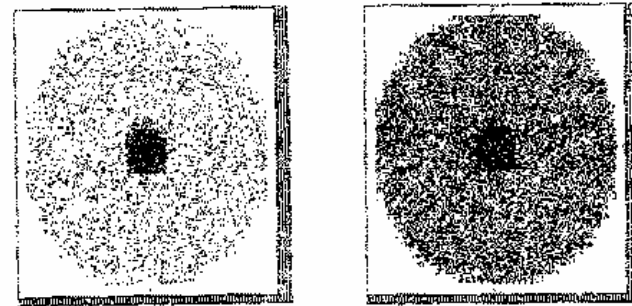
Fig. 40. Contrast resolution of a CT-image at 40 keV (high contribution of photoelectric effect) and 200 keV (high contribution of Compton effect).

Fig. 39. Linear attenuation coefficient μ (cm^{-1}) versus electron density δ_e at 60 keV ($\triangle$), 120 keV ($\Diamond$) and 250 keV ($\square$). A linear correlation can be observed, following eq. (45), at 250 keV only, where photoelectric contribution is negligible.

Table 5
Attenuation coefficients μ_1 and μ_2 (cm^2/g) close to the energy of the photoelectric discontinuities (in keV) for Cu, Ag, I and Pb

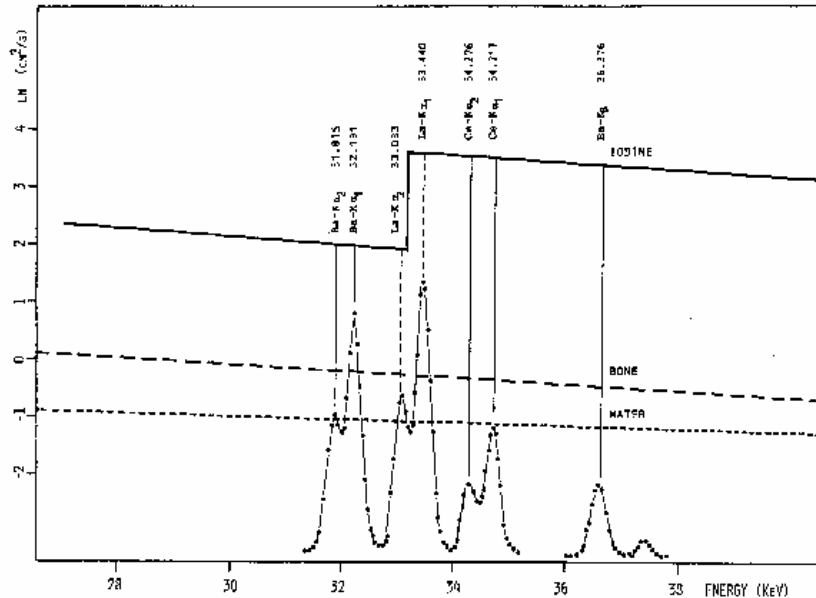| Element	Energy of the discontinuity (keV)	μ_1	μ_2	μ_2 / μ_1
Cu	8.98 (K)	26	285	237
Ag	25.52 (K)	9.7	52	42
I	33.16 (K)	7.5	32.5	25
	13.04 (L$_{III}$)	73	153	80
Pb	88.0 (K)	1.8	6.6	4.8
	15.87 (L$_I$)	136	141	5
	15.21 (L$_{II}$)	113	143	30

Fig. 41. Attenuation coefficient of iodine, showing the K-discontinuity, and position of the energy values of X-rays of barium, lanthanum and cerium, useful for the differential tomography of iodine.

3.2.1. Theoretical background

We start by considering a matrix of thickness x containing an element a with concentration c_a. If we use a beam of X-rays made up to two energies E_1 and E_2, which bracket the photoelectric edge of the element a, the attenuation is given by

$$N_1 = N_{01} \exp\{[\mu_{m1}(1 - c_a) + \mu_{a1} c_a]x\} ,$$

$$N_2 = N_{02} \exp\{-[\mu_{m2}(1 - c_a) + \mu_{a2} c_a]x\} .$$

(43)

In eq. (43) N_{01}, N_{02}, N_1 and N_2 represent the intensities of the incident and transmitted radiation at energies E_1 and E_2, respectively. μ_{m1}, μ_{m2}, μ_{a1} and μ_{a2} represent the attenuation coefficients of the matrix and of element a at energies E_1 and E_2, respectively. The ratio $R = N_2/N_1$ can be written as

$$R = \frac{N_{02}}{N_{01}} \frac{\exp\{-[\mu_{m1} - c_a(\mu_{m1} - \mu_{a1})]x\}}{\exp\{-[\mu_{m2} - c_a(\mu_{m2} - \mu_{a2})]x\}} , \qquad R = R_0 \exp[(\Delta\mu_m \cdot c_a(\Delta\mu_m - \Delta\mu_a)x] ,$$

$$R_0 = N_{02}/N_{01} , \quad \Delta\mu_m = (\mu_{m1} - \mu_{m2}) , \quad \Delta\mu_a = (\mu_{a1} - \mu_{a2}) .$$

(44)

Close to the edge $\mu_{m1} - \mu_{m2} \approx 0$, $\mu_{a2} - \mu_{a1} > 0$ and therefore, $\Delta\mu_m < \Delta\mu_a$. If $\Delta\mu_a \gg \Delta\mu_m$, then

$$R = R_0 \exp(\Delta\mu_a c_a x) .$$

(45)

Differential tomography therefore depends only on the concentration c_a of the element to be analyzed. One can calculate that the sensitivity of the method ranges between 300 and 400 ppm, for medium atomic-number elements [112], which is much better than the sensitivity of "ordinary" transmission tomography.

3.2.2. Results

Tomographs have been carried out at energies above and below the K-discontinuity of silver and iodine [110]. For silver, which has the K-discontinuity at 25.517 keV, secondary targets of tin ($K_\alpha = 25.15$ keV) and antimony ($K_\alpha = 26.2$ keV), have been employed to obtain monoenergetic characteristic radiation. In fig. 42 results of differential tomographs carried out on a plexiglas cylinder with two holes filled with Ag solutions at 4% and 2% are shown. For iodine, which has the K-discontinuity at 33.164 keV, various pairs have been examined: Ba-K_α (32 keV) and Ba-K_β (36.4 keV); Ba-K_α (32 keV) and Ce-K_α (34.5 keV); La-$K_{\alpha2}$ (33.033 keV) and La-$K_{\alpha1}$ (33.44 keV). Tomographs using the last pair are shown in fig. 43.

The same principles have been applied by Fryar et al. [111, 112]. They first employed a 3 mCi Cd 109 source emitting silver X-rays (22 and 25.2 keV) for imaging palladium (K-edge 24.4 keV between K_α and K_β Ag lines). They also used secondary X-rays emitted from barium excited by an Am 241 source for detecting cesium. In a more recent work, they also employed an X-ray tube and filtered the bremsstrahlung radiation with tin foils, for producing selective images of palladium, silver and cadmium [112]. A series of images of a sample of epoxy glue containing the three elements Pd, Ag and Cd separately, at a concentration of about 10–25 mg/cm³ was shown in fig. 44 [112].

3.3. Compton tomography

As was shown in section 2.3, and in particular section 2.3.4, analytical information can be extracted from the scattered photon distribution. When using Compton-scattered radiation, two aspects can be considered: the energy shift of the Compton peak as a function of energy and scattering angle (see for
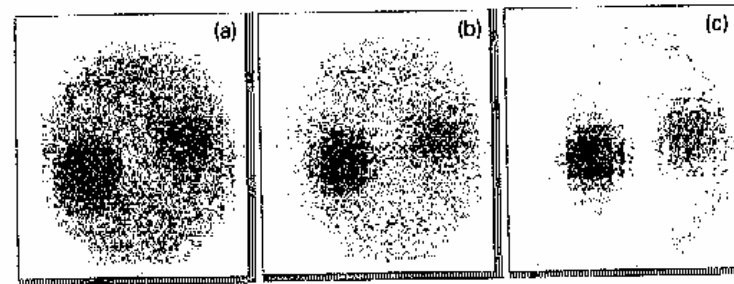

Fig. 42. Differential tomography of a plexiglas cylinder with two cylindrical holes filled with 4% and 2% silver in water solution: (a) tomography at 25.15 keV (Sn-target). (b) tomography at 26.2 keV (Sb-target). (c) (b − a) differential tomography.
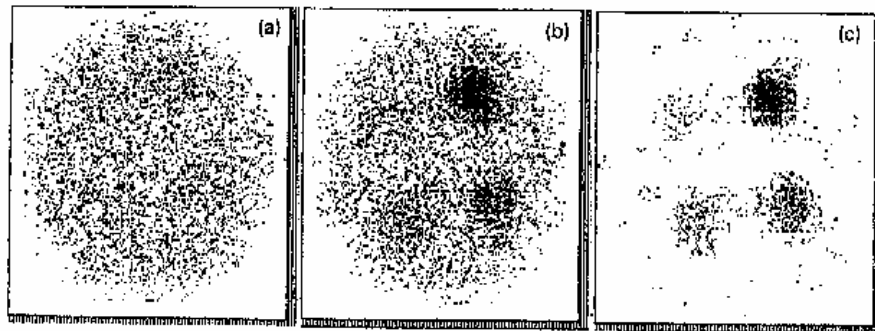
Fig. 43. Differential tomography of a plexiglas cylinder with four cylindrical holes filled with 4%, 2%, 1% and 0.5% iodine in water solution. (a) tomography at 33.033 keV, (b) tomography at 33.44 keV, (c) (b − a) = differential tomography.
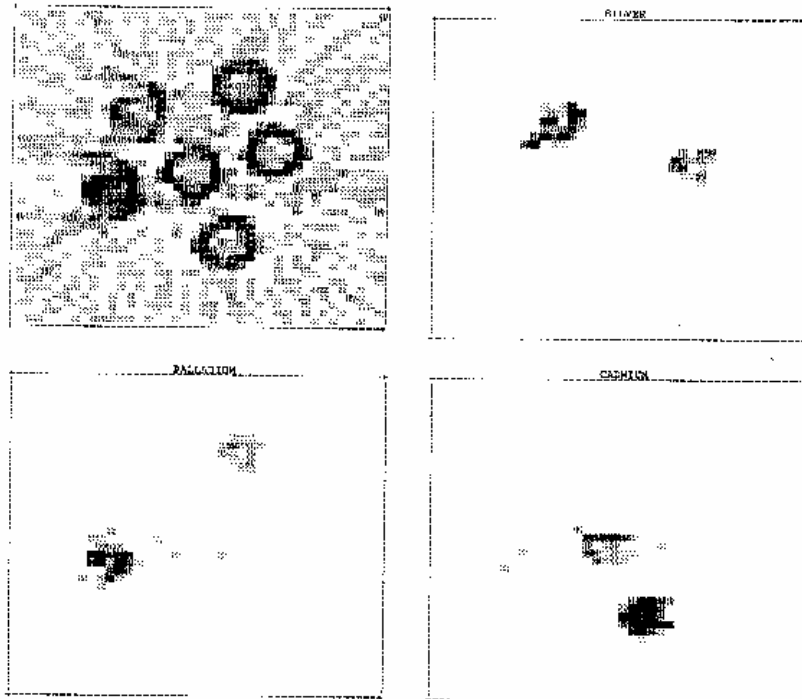

Fig. 44. Upper left: "normal" tomography of the test object containing Pd, Ag and Cd. Lower left: differential tomography of Pd. Upper right: differential tomography of Ag. Lower right: differential tomography of Cd.

example fig. 17), and the Compton differential cross sections. Energy discrimination is necessary for selecting the Compton peak, and the energy separation between the coherent and Compton peaks increases with the angle. The Compton differential cross section has a maximum at 90°. Further, the intensity of the Compton-scattered radiation at the detector is proportional to the electron density ρ_e, see eqs. (38) and (41b). Therefore, the reconstructed image should reflect an "electron density image". Further, one problem is the shape of the irradiated volume element (voxel) of the sample due to the source and detector geometry.

Attempts to use Compton-scattered photons to produce medical images are reported by Farmer and Collins [85], Huddleston and Bhaduri [74], Battista and Bronskill [114], Guzzardi and Mey [115]. They all used a 90° geometry. Guzzardi and Mey employed a fan beam of 279 keV γ-rays from an 80 cm linear source of Hg 203 (halflife of 47 days) for irradiating a selected coronal chest section. The detecting device was a gamma camera positioned over the patient's chest with the detector plane parallel to the incident beam. In this way the system was able to detect the radiation scattered into 90°, having a Compton energy of 181 keV. After correction for the effects of attenuation and multiple scattering within the patient, the linearity of counts versus density was evaluated (fig. 45). The performance of the system in terms of spatial resolution and density-gradient discrimination is limited, but it could provide a medium spatial resolution method for detecting the overall distribution of lung density. Hence it could be suitable for monitoring changes in lung pathology.

A different approach to Compton scatter imaging was taken by Brateman et al. [116], Harding and Tischler [117] and Harding and Kosanetzky [118]. They detect the back-scattered photons by means of one or more detectors symmetrically placed with respect to the incident beam. Harding and Kosanetzky [118] developed a system called COMSCAN-Philips, for Compton back-scatter tomography of low atomic-number materials. The authors observed that the spatial distribution of the scattered photons was approximately isotropic (except in the forward direction) for incident energies larger than a few tens of keV (see figs. 4–10). A practical consequence is the free choice of the imaging geometry. The intensity of radiation scattered from a volume element (voxel) dV inside the irradiated object can be expressed as

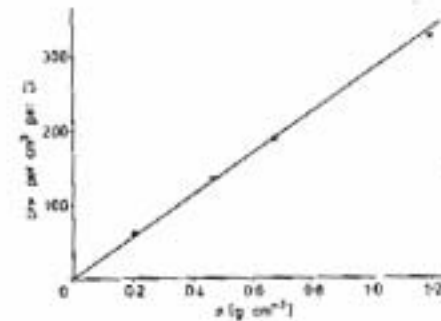$$N_C = \rho_r \, dV \exp(-\mu_p x) \exp(-\mu_s x') + M \,. \tag{46}$$

Fig. 45. Count-density relationship for 90° Compton-scattering tomography.

The two exponentials describe the beam attenuation along the path of the primary beam x, as well as the scattered radiation path x', with $\mu_2 \approx \mu_0$, due to the energy shift of the Compton-scattered photons. The last term M originates from multiple scattering processes.

It is interesting to compare the contrast of the transmission system with that of the back-scatter system. Considering an object of size x whose attenuation coefficient is equal to μ except in a small void region (size Δx) (fig. 46), the transmitted intensities are

$$N_T = N_0 \exp(-\mu x), \qquad N_{T'} = N_0 \exp[-\mu(x - \Delta x)], \qquad (47)$$

for the regions not including x and including x, respectively. If the contrast C of the small defect is small enough to ensure the replacement of the exponential function by its linear expansion, C can be written as

$$C = (N_{T'} - N_T)/N_1 = \exp(\mu \Delta x) - 1. \qquad (48)$$

If the defect is small enough to ensure the replacement of the exponential function by its linear expansion, this results in $C = \mu \Delta x$. Thus, in transmission systems the contrast is proportional to the defect size.

In the back-scatter system (fig. 47), the intensities are given by

$$N_s = (\Delta x)^3 \mu F_p F_s K, \qquad N_{s'} = (\Delta x)^3 \mu' F_p F_s K, \qquad (49)$$

where F_p and F_s are the attenuation of primary and scatter radiation and K is a geometrical factor. The contrast is therefore given by $C = \Delta \mu/\mu$, and is independent of the defect size. For example, if we consider an air bubble in aluminium, probed with 60 keV X-rays, $m_{Al} = 0.28 \, cm^2/g$, and with transmission measurements the smallest defect detectable with 10% contrast is $\Delta x = 3.5 \, mm$. By using the back-scatter method, we get a contrast which is nearly 7% irrespective of the defect size.

The COMSCAN has found applications in several areas (light metal alloys, laminated and plastics) with the limitation of a near-surface region. Further, it can be employed with a free choice of the imaging geometry. Therefore, large bulky objects can be inspected, without any problem, just from one side.
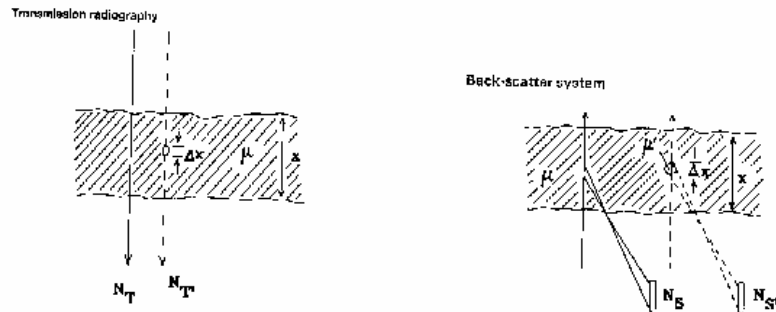

Fig. 46. Count-density relationship for the contrast calculation of transmission methods.

Fig. 47. Count-density relationship for the contrast calculation of back-scatter system.

3.4. Coherent-scatter computed tomography

Referring to figs. 4 to 10, it is evident that the predominant component of very small-angle scatter is actually coherent scattering. Coherent scattering is important in the small-angle region because the differential cross section increases in the forward direction and because the small-angle Compton scattering is inhibited due to electron binding effects. For example, consider 10 keV photons interacting with a water sample; the differential coherent cross section at 10% is about $4 \times 10^{-23} \, cm^2$, and the differential Compton cross section about $8 \times 10^{-26} \, cm^2$. At 180° the situation is inverted, the differential coherent cross section is about $2 \times 10^{-25} \, cm^2$ and the differential Compton cross section about $5 \times 10^{-25} \, cm^2$.

The dependence of the differential coherent cross section on the atomic number Z of the scattering material is an expression of the type $(d\sigma/d\Omega)_{coh} \propto Z^n$ (see fig. 48) where n sharply increases with the scattering angle.
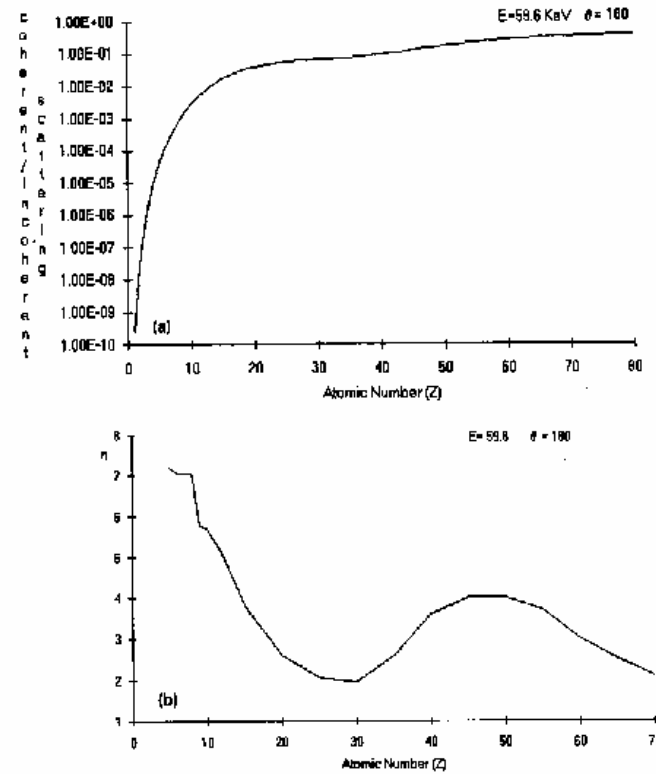

Fig. 48. (a) Ratio R/C of coherent to Compton radiation at $E_0 = 59.6$ keV and scattering angle $\theta = 180°$ versus atomic number Z; (b) dependence of coherent counts versus atomic number; the factor n has been calculated from (a).

As observed in section 2.3.1, a new imaging method using small-angle coherent scattering has been developed by Harding and coworkers [117–119]. The measurement system is shown in fig. 49. The radiation source was a W anode tube, operated at 120 kV and 5 mA with 0.4×0.4 mm^2 focal spot. The transmitted and scattered radiations falling within a gap of half-angle 6° are recorded by an array of scintillation detectors (BGO) operating in current integration mode. The primary beam and the detector array were fixed, and the object and the calibration block were mounted on a translation stage, which provided the movement required to accumulate the data for one projection. The object was mounted on a standard translation rotation stage. Figure 50 shows the phantom transmission image and nine scatter images. A standard phantom of the American Association of Physicists in Medicine was used.

3.5. Fluorescence X-ray (XRF) tomography

This type of tomography, also called X-ray microscopy, is based on the detection of the fluorescent X-rays emitted by a sample containing elements with medium or high atomic number [120]. The principle of the method is shown in fig. 51. The output of the X-ray tube is strongly collimated delimiting the object to be scanned as a section of a conical volume. The detector, which analyzes the X-rays emitted from the irradiated volume, is placed at 90° with respect to the primary radiation. It is also strongly collimated like the X-ray output. The intersection of the solid angles of both collimators identifies a fixed volume in the object. By moving the object in the x–y direction, the X-ray intensity of elements present in the sample can be mapped, and finally an image can be obtained related to the distribution of the element or of the elements in the sample.

3.5.1. Theoretical background

Let us consider a sample containing an element a, with concentration c_a, irradiated with N_0 photons with energy E_0 in a 90° geometry. One can divide the section of the sample into many viewing elements (pixels) in which the attenuation of incident and output radiation is negligible. For pixels of about 1–2 mm^2 and elements with atomic number larger than about 40, each pixel can be considered as an
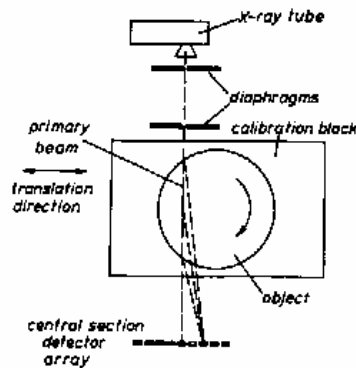

Fig. 49. Schematic illustration of the measurement system for X-ray diffraction tomography (from Harding et al. [118]).
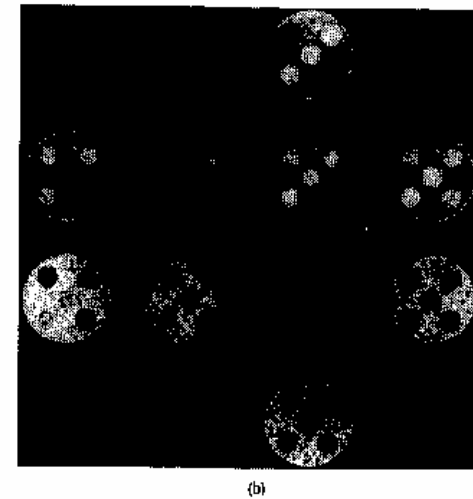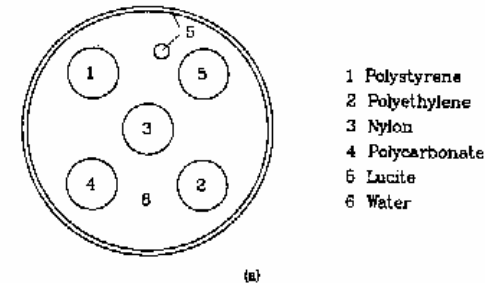
AAPM CONTRAST PHANTOM

1 Polystyrene
2 Polyethylene
3 Nylon
4 Polycarbonate
5 Lucite
6 Water

(a)

(b)

Fig. 50. (a) Form and composition of the CT performance phantom. (b) Transmission CT-image of the phantom. Scatter image of the phantom at (top left to bottom right) 1.5, 1.7, 2.7, 3.3, 4.1, 4.5, 5.0, 6.10 (from Harding et al. [118]).

infinitely thin sample, and X-rays emitted into 90° are given by

$$N_a = N_0 K \omega_a \mu_{ph, a}(E_0) 0.7 m c_a , \tag{50}$$

which is similar to eq. (26c), except for the value 0.7, which depends on the angle. The parameters of eq. (50) have been listed in table 1. There is a linear relationship between the concentration c_a and the characteristic X-rays from element a, N_a.

The number of scattered photons is $N_{sc} = N_0 K \mu_{sc} m$. The ratio between photoelectric and scattered
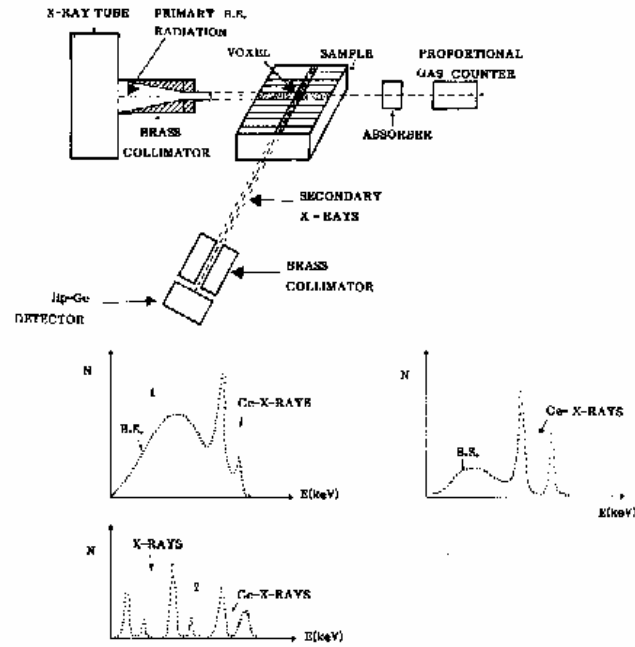
efficiency is low, $K = \Omega_1\Omega_2 - 1.3 \times 10^{-8}$; so a very strong source is needed. The irradiated volume varies with the distance between the sample and both the source and the detector. It is therefore necessary to keep constant the position of the volume by moving the sample in the x–y intersection point. X-ray counts of element a have to be corrected for attenuation effects, both of incident and output radiation from the irradiated pixel.

A test object has been analyzed, constituted by a plexiglas matrix $20 \times 20\,mm^2$ section, with 64 cylindrical holes of diameter 2 mm. The holes are empty, except those on the diagonal of the object, which are filled with a solution containing 0.5% iodine (fig. 52). Further, measurements have been carried out on a plexiglas sample with several Cu wires disposed vertically in the sample (fig. 53a) and on an epoxy resin sample containing a small Ag grain (fig. 53b). Finally, the diffusion of Ag ions through a LiF crystal was studied, after doping the LiF crystal with a small quantity of AgI, and heating at 600 °C for 24 hours (figs. 54).

Bavdaz et al. [121] used synchrotron radiation as a more collimated, high-intensity source to map elements in a low-Z matrix. The advantages of using synchrotron radiation instead of X-ray tubes lies

Fig. 51. Experimental set-up for XRF-tomography. The primary radiation is highly collimated (when iodine is analyzed the collimator is covered by a Ce-mixture for improving the intensity). The collimators select, in a geometrical way, the radiation emitted at 90° by the sample. The intersection of collimated primary and fluorescent radiations defines a volume element called voxel. Typical primary and secondary spectra are also shown (1 and 2), and transmitted spectrum (3).

counts is given by

$$N_a/N_{sc} = \omega_a \mu_{ph,\,a} 0.7 c_a/\mu_{sc}. \tag{51}$$

The sensitivity of the technique, both in the single-point and in the tomographic version, is of the order of ppm, which must be compared with hundreds of ppm of the differential tomography, and with thousands of ppm in the case of normal transmission tomography.

3.5.2. Experimental set-up and measurements

The experimental arrangement employed for the analysis of iodine has been shown in fig. 51. The bremsstrahlung radiation from the X-ray tube passes through a collimator 6 cm long and 1 mm diameter, internally coated with Ce, in order to partially convert the primary radiation to Ce X-rays, whose energy lies just above the iodine K-edge. The detector (a HpGe having 900 eV resolution at the iodine X rays) is also collimated, with a collimator 6 cm long and 1 mm diameter. A fixed volume of approximately $0.5 \times 0.6 \times 0.5\,mm^3$ is therefore analyzed. With this geometrical arrangement, the
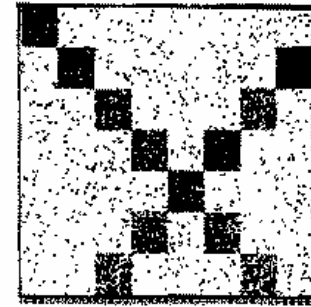

Fig. 52. XRF tomography of a test object on plexiglas, with holes on the diagonal, filled with a solution containing 0.5% iodine.
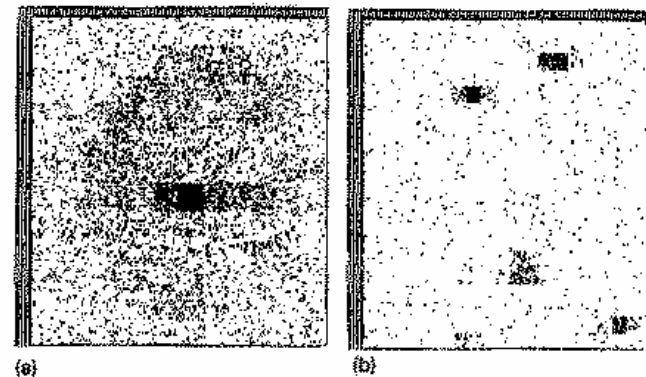

Fig. 53. (a) XRF tomography of an object containing epoxy resin mixed with a Ag grain (in the middle). The scanned surface is about $6 \times 6\,mm^2$. (b) XRF tomography of a plexiglas object containing Cu wires disposed vertically. The scanned section is about $8 \times 8\,mm^2$.
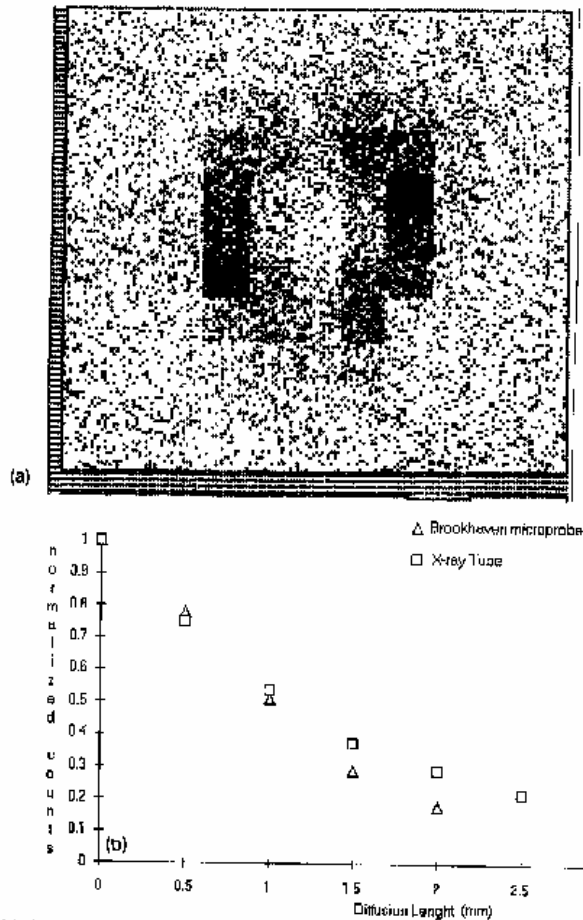
Fig. 54. (a) Diffusion of Ag ions through a LiF crystal. A AgI solution was put into a cylindrical hole drilled in the center of the crystal, which was then heated at 600°C for 24 h. The solution was then removed from the hole, and the Ag content measured in a section of the crystal orthogonal to the drilled cylinder, by means of the fluorescence X-ray tomography. (b) Ag content along a diagonal line of the section described in a), determined with an X-ray tube (□) and with synchrotron radiation (△).

Fig. 55. XRF tomography of nickel grains in an organic polymer matrix.

Fig. 56. Distribution of gallium in foetal rat bone taken with the collimated X-ray microscope. The lowest picture is a photomicrograph showing the region scanned. The top two displays show the Ga-distribution in terms of a contour plot (top) and a density plot (center). The pixel size in the map is 40 μm × 40 μm (after Jones [122]).

mainly in the high photon flux. Very small samples were scanned (<500 μm) with a spatial resolution down to 3 μm. An image of nickel gains in a polymer matrix is shown in fig. 55. Also Jones et al. [122] and Gohshi et al. [123] employed synchrotron radiation for mapping trace elements in microscopic samples. Jones et al. have used both a collimated X-ray beam with sizes down to around 20 μm, and a focussed 10 keV X-ray beam. They employed a standard reference sample produced by adding a number of elements to gelatin at a concentration level of 10 ppm by wet weight, for measuring the
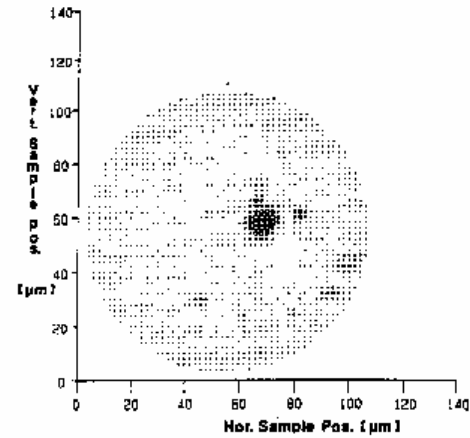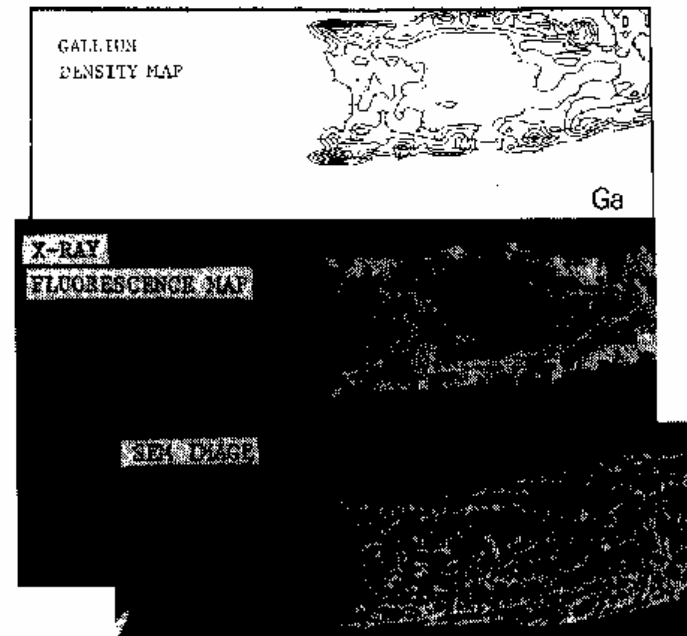
minimum detection limits for fluorescent X-ray peaks. Minimum detection limits about 10 fg have been obtained. A map made of the gallium distribution in a 20 μm section of fetal rat bone is shown in fig. 56. Gohshi et al. employed a focussed beam of photons with energies up to 10 keV, with a spatial resolution better than 10 μm for analyzing low atomic-number elements like Zn, Mn and Ca absorbed in chelate resins.

4. Conclusions

The last two decades have seen a great increase in the studies, both theoretical and experimental, directly or indirectly related to the general subject of interaction of radiation with matter. This phenomenon, which is continuing or intensifying at present, is due to the following main reasons. The development of the computed tomography (CT) scanner by Hounsfield in 1971. CT-tomography is based on a large number of transmission measurements and its characteristics depend on the type of interaction between the X-rays and the sample. In addition to transmission tomography, more recently also Compton-scattered radiation at about 90° and back-scatter radiation were employed for imaging a sample, and in the last few years also small-angle Rayleigh-scattered radiation. Finally, fluorescent X-rays emitted by medium and heavy elements of the sample have been employed for selectively mapping the distribution of the element itself. All of the methods described above take advantage of careful studies of the interaction of X-rays with matter, accurate knowledge of interaction cross sections versus angles and atomic number and semiempirical formulae of attenuation coefficients.

In general, different CT-scanners are used for transmission measurements, for Compton tomography, for Rayleigh small-angle tomography and for X-ray microscopy. In this review article, we propose to realize a scanner using at the same time various detectors for collecting all different types of information (see fig. 15).

– The introduction of research in synchrotron radiation. Many synchrotron-radiation facilities have been constructed and a large number of new facilities are being built throughout the world. Synchrotron radiation has stimulated theoretical and experimental work in many fields, like material science X-ray imaging, analytical techniques like X-ray fluorescence, X-ray diffraction studies, X-ray absorption fine-structure spectra, Compton-profile methods and others.

– The large availability of new detectors characterized by high energy resolution and intrinsic stability, like semiconductor detectors (cooled at nitrogen temperature like Ge and Si, or at room temperature like HgI_2) led to a great increase of basic and applied research.

– The increasing interest in the field called "nuclear analytical techniques" including energy-dispersive photon or proton induced X-ray fluorescence, Rayleigh to Compton ratio and others. The first methods are largely employed in many fields for major and trace element analysis, the second typically for densitometric determinations.

Experimental studies of the Rayleigh to Compton ratio showed, in particular, that the theory of the Rayleigh effect and detailed Rayleigh-scattering calculations based on the "atomic form factor" are not satisfactory. Also studies on Compton profile are very interesting for the possibility they offer to distinguish and differentiate between different materials. In the future we play to start a very systematic study on the correlation between Compton profile and composition of the scattered material.

All the equipment, methods and techniques discussed are based on the various types of interaction of radiation with matter. For example X-ray microscopy, which is a field that has developed rapidly in recent years, implies focusing and collimation of radiation, monochromatizing of the incident X-ray

beam, study of the photoelectric effect in the sample, and so on. We plan, in the future to improve on these studies, both from a theoretical and from an experimental point of view. In conclusion, we are convinced that there is still a large area to be explored in the interaction of X-rays with matter, from a theoretical and, more important, from an experimental point of view. In the coming years we will see a further improvement in this area and the development of more sophisticated instrumentation for imaging and for analytical applications.

References

[1] P. Marmier and E. Sheldon, Physics of Nuclei and Particles, Vol. VI (Academic Press, New York, 1969) chap. 4.
[2] C.P. Lin, K.T. Cheng and W.R. Johnson, Phys. Rev. A 11 (1975) 1946–1956.
[3] W.R. Johnson and F.D. Feiock, Phys. Rev. 168 (1968) 22 23.
[4] L. Kissel, R.H. Pratt and S.C. Roy, Phys. Rev. A 22 (1980) 1970 2004.
[5] P.P. Kane, L. Kissel, R.H. Pratt and S.C. Roy, Phys. Rev. 140 (1986) 75–159.
[6] D.T. Cromer and J.T. Waber, Acta Cryst. 18 (1965) 104 109.
[7] D.T. Cromer and J.B. Mann, Acta Cryst. A 24 (1968) 321 324.
[8] J.R. Mossop, S.A. Kerr, D.A. Bradley, C.S. Chong and A.M. Ghose, Nucl. Instrum. Methods Phys. Res. A 255 (1987) 419–422.
[9] U. Bonse and G. Materlik, Z. Phys. B 24 (1976) 189 191.
[10] L.K. Templeton, D.H. Templeton and R.P. Phizackerley, J. Am. Chem. Soc 102 (1980) 1185–1186.
[11] D.T. Cromer and D.A. Liberman, Acta Cryst. A 37 (1981) 267 276.
[12] M. Hart and D.P. Siddons, Proc. R. Soc. London A 376 (1981) 465 482.
[13] G. Basavaraju, L. Kissel, J.C. Parker, R.H. Pratt, S.C. Roy and S.K. Ken Gupta, Phys. Rev. A 34 (1986) 1905.
[14] P. Drier, P. Rabe, W. Malzfeldt and W. Niemann, J. Phys. C 17 (1984) 3123 3136.
[15] J. Bremer, J. Phys. B 12 (1979) 2797–2807.
[16] D.H. Templeton and L.K. Templeton, Acta Cryst. A 36 (1980) 436 442.
[17] K.G. Tirsell, V.W. Slivinsky and P.J. Ebert, Phys. Rev. A 12 (1975) 2426–2437.
[18] J.H. Hubbell, W.J. Weigele, E.A. Biggs, R.T. Brown, D.T. Cromer and R.J. Howerton, J. Phys. Chem. Ref. Data 4 (1975) 471–616.
[19] D.T. Cromer and J.B. Mann, J. Chem. Phys. 47 (1967) 1982–1983.
[20] D.T. Cromer, J. Chem. Phys. 50 (1969) 4857–4859.
[21] M.A. Stroscio, Phys. Rev. A 29 (1984) 1691–1694.
[22] M.K. Prasad, D.S. Kershaw and J.D. Beason, Appl. Phys. Lett. 48 (1986) 1193–1195.
[23] R. Ribberfors, Phys. Rev. B 12 (1975) 2067–2074.
[24] R. Ribberfors, Phys. Rev. B 12 (1975) 3136–3141.
[25] R. Ribberfors and K.F. Berggren, Phys. Rev. A 26 (1982) 3225–3333.
[26] F. Biggs, L.B. Mendelsohn and J.B. Mann, At. Data Nucl. Data Tables 16 (1975) 201 309.
[27] I.R. Whittingham, J. Phys. A 4 (1971) 21.
[28] P. Froelich and W. Weyrich, J. Chem. Phys. 80 (1984) 3669.
[29] N.C. Bacalis, N.I. Papanicalaou and D.A. Papaconstantopoulos, J. Phys. F 16 (1986) 1471.
[30] M.J. Cooper, D. Laundy, D.A. Cardwell, D.N. Timms, R.S. Holt and G. Clark, Phys. Rev. B 34 (1986) 5984 5987
[31] G.E.W. Bauer and J.R. Schneider, Phys. Rev. B 31 (1985) 681–692.
[32] B.W. Loo, F.S. Goulding and D.S. Simon, IEEE Trans. Nucl. Sci. 33 (1986) 531.

[33] W.A. Reed, P. Eisenberger, K.C. Pandey and P.C. Snyder, Phys. Rev. 309 (1974) 1507–1515.
[34] I. Theodoridou and N.G. Alexandropoulos, Z. Phys. B 54 (1984) 225–228.
[35] K. MacKenzie, D.G. Williams, T.G. Sparrow and J.R. Stone, Proc. R. Soc. London A 389 (1983) 485.
[36] N.I. Papanicolaou, N.C. Bacalis and D.A. Papaconstantopoulos, Z. Phys. B 65 (1987) 453–464.
[37] Y. Kubo and S. Wakoh, J. Phys. F 17 (1987) 397–408.
[38] M. Causa, R. Dovesi, C. Pisani and C. Roetti, Phys. Rev. B 34 (1986) 2939–2941.
[39] N.I. Papanicolaou, N.C. Bacalis and D.A. Papaconstantopoulos, Phys. Status Solidi b 137 (1986) 597–606.
[40] M. Blume, J. Appl. Phys. 57 (1985) 3615–3618.
[41] M. Blume and D. Gibbs, Phys. Rev. B 37 (1988) 1779–1789.
[42] R.S. Holt and M. Cooper, Nucl. Instrum. Methods Phys. Res. 213 (1983) 447–452.
[43] R.S. Holt, D. Laundy, D.A. Cardwell, M. Cooper, T. Naylor, S. Manninen and P. Hatton, Nucl. Instrum. Methods Phys. Res. A 243 (1986) 608–618.
[44] M.J. Cooper, Adv. Phys. 20 (1971) 453–491.
[45] W.H. McMaster, N.K. Del Grande, J.H. Mallet and J.H. Hubbell, Vols. 1, 2, 3 and 4 UCRL-50174 (1969).
[46] D. Schaupp, M. Schumacher, F. Smend, P. Rullhusen and J.H. Hubbell, J. Phys. Chem. Ref. Data 12 (1983) 467–512.
[47] J.H. Hubbell and I. Overbo, J. Phys. Chem. Ref. Data 9 (1979) 69–105.
[48] J. Kosanetzky, G. Harding, K.H. Fischer and A. Meyer, Philips Techn. Inform. (1988).
[49] A.L. Hanson, Nucl. Instrum. Methods Phys. Res. A 234 (1985) 552–555.
[50] A.L. Hanson, Nucl. Instrum. Methods Phys. Res. A 243 (1986) 583–598.
[51] A.L. Hanson, Nucl. Instrum. Methods Phys. Res. A 249 (1986) 515–522.
[52] A.L. Hanson, Nucl. Instrum. Methods Phys. Res. A 249 (1986) 522–539.
[53] A.L. Hanson, Nucl. Instrum. Methods Phys. Res. A 260 (1987) 264–275.
[54] A.L. Hanson, Nucl. Instrum. Methods Phys. Res. A 264 (1988) 471–483.
[55] A.L. Hanson, Nucl. Instrum. Methods Phys. Res. A 264 (1988) 484–487.
[56] A.L. Hanson and M. Meron, Nucl. Instrum. Methods Phys. Res. A 264 (1988) 488–496.
[57] R. Cesareo, Nucl. Instrum. Methods Phys. Res. 179 (1981) 545.
[58] G. Matscheko, G.A. Carlsson and R. Ribberfors, Phys. Med. Biol. 34 (1989) 199.
[59] E. Gatti, P. Rehak and J. Kemmer, IEEE Trans. Med. Imaging 5 (1986) 207.
[60] J. Sherman, Spectrochim. Acta 7 (1955) 283; 14 (1959) 466.
[61] T. Shiraiwa and N. Fujino, Jap. J. Appl. Phys. 5 (1966) 886.
[62] C.E. Webber and T.J. Kennet, Phys. Med. Biol. 21 (1976) 760.
[63] R.L. Clarke and G. Van Dyk, Phys. Med. Biol. 18 (1973) 532.
[64] T. Pitkanen, A. Laundy, R.S. Holt and M.J. Cooper, Nucl. Instrum. Methods Phys. Res. A 251 (1986) 536.
[65] T. Pitkanen, M.J. Cooper, A. Laundy and R.S. Holt, Nucl. Instrum. Methods Phys. Res. A 257 (1987) 384.
[66] R. Cesareo, in: Nuclear Analytical Techniques in Medicine, ed. R. Cesareo (Elsevier, Amsterdam, 1988) chap. 2, pp. 19–121.
[67] L.A. Currie, Anal. Chem. 40 (1968) 586.
[68] A.L. Hanson, H.W. Kramer, K.W. Jones, B.M. Gordon, R.E. Mills and J.R. Chen, IEEE Trans. Nucl. Sci. NS-30 (1983) 1339.
[69] L. Kaufman, in: Medical Applications of Fluorescent Excitation Analysis, eds L. Kaufman and D.C. Price (CRC Press, Boca Raton, 1979) p. 91.
[70] C.J. Sparks, Jr, in: Synchrotron Radiation Research, eds H. Winick and S. Doniach (Plenum Press, New York, 1980) p. 459.
[71] J.O. Christoffersson and S. Mattsson, Phys. Med. Biol. 28 (1983) 1135.
[72] R. Jonson and B. Unsgaard, Phys. Med. Biol. 33 (1988) 847.
[73] E.S. Garnett, T.J. Kennett, D.B. Kenyon and C.E. Webber, Radiology 10 (1973) 209.
[74] A.L. Huddleston and D. Bhaduri, Phys. Med. Biol. 24 (1979) 310.
[75] H. Olkkonen and P. Karjalainen, Br. J. Radiol. 48 (1975) 594.
[76] A.L. Huddleston and J.B. Weaver, Int. J. Appl. Radiat. Isot. 34 (1983) 997.
[77] C.E. Webber and G. Coates, Med. Phys. 9 (1982) 473.
[78] P.G. Lale, Phys. Med. Biol. 4 (1959) 159.
[79] P.G. Lale, Radiology 90 (1968) 510.
[80] R. Guzzardi, M. Mey, M. Pistolesi, S. Solfanelli and C. Giuntini, J. Nucl. Med. Allied. Sci. 22 (1978) 11.
[81] H.L. Cox and P.S. Ong, Med. Phys. 4 (1977) 99.
[82] M.J. Cooper, A.J. Rollason and R.W. Tuxworth, J. Phys. E 15 (1982) 568.
[83] P.C. Shrimpton, Phys. Med. Biol. 26 (1981) 907.
[84] G. Coates and C.E. Webber, Med. Phys. 9 (1982) 478.
[85] P.T. Farmer and M.P. Collins, Phys. Med. Biol. 16 (1971) 577.
[86] J. Felsteiner and P. Pattison, Nucl. Instrum. Methods Phys. Res. 124 (1975) 449–453.
[87] I. Arino and H.P. Gardner, J. Radioan. Chem. 54 (1979) 221.
[88] G.E. Gigante and A.L. Hanson, private communication (1989).

[89] A.L. Hanson and G.E. Gigante, Phys. Rev. 40 (1989) 171–180.
[90] H. Kunzendorf, Nucl. Instrum. Methods 99 (1972) 611.
[91] P. Puumalainen, A. Uimarihuhta, E.M. Alhava and H. Olkkonen, Radiology 120 (1976) 723; P. Puumalainen, H. Olkkonen and P. Sikanen, Int. J. Appl. Radiat. Isot. 28 (1977) 785.
[92] H.P. Schatzler, Int. J. Appl. Radiat. Isot. 30 (1979) 115.
[93] P. Puumalainen, H. Olkkonen and P. Sikanen, Nucl. Instrum. Methods 163 (1979) 261.
[94] S.A. Kerr, K. Kouris, C.E. Webber and T.J. Kennet, Phys. Med. Biol. 25 (1980) 1037–1047.
[95] J.T. Stalp and B. Mazess, Med. Phys. 7 (1980) 723.
[96] S.S. Ling, S. Rustgi, A. Karellas, J.D. Craven, J.S. Whiting, M.A. Greenfield and R. Stern, Med. Phys. 9 (1982) 208.
[97] I. Leichter, A. Karellas, J.D. Craven and M.A. Greenfield, Med. Phys. 11 (1984) 31.
[98] A. Karellas, I. Leichter, J.D. Craven and M.A. Greenfield, Med. Phys. 10 (1983) 605.
[99] M.A. Greenfield, J.D. Craven, S.S. Shukla, A. Karellas and I. Leichter, Med. Biol. Eng. Comput. 23 (supplement) (1985) 1074.
[100] G.E. Gigante and S. Sciuti, Med. Phys. 12 (1985) 321.
[101] G.E. Gigante and S. Sciuti, Int. J. Appl. Radiat. Isot. 35 (1984) 481.
[102] P. Puumalainen, A. Uimarihuhta, H. Olkkonen and E.M. Alhava, Phys. Med. Biol. 27 (1982) 425.
[103] M.J. Cooper, R.S. Holt and R.S. Harding, J. Phys. E 18 (1985) 354.
[104] D.N. Timms, M.J. Cooper and R.S. Holt, J. Phys. E 20 (1987) 76.
[105] M.J. Cooper, Contemp. Phys. 18 (1977) 489.
[106] G.E. Gigante, L.J. Pedraza and S. Sciuti, Nucl. Instrum. and Methods Phys. Res. B 12 (1985) 229.
[107] C. Bui, M. Milazzo and M. Monichino, Nucl. Instrum. Methods Phys. Res. B 28 (1987) 88.
[108] S. Manninen, T. Pilkuuen, S. Koikkalainen and T. Paakkari, Int. J. Appl. Radiat. Isot. 35 (1984) 93.
[109] S. Manninen and S. Koikkalainen, Int. J. Appl. Radiat. Isot. 35 (1984) 95–99.
[110] R. Cesareo, Nucl. Instrum. Methods Phys. Res. A 270 (1988) 572.
[111] J. Fryar, K.J. McCarthy and A. Fenelon, Nucl. Instrum. Methods Phys. Res. A 259 (1987) 557.
[112] J. Fryar, K.J. McCarthy and A. Fenelon, Nucl. Instrum. Methods Phys. Res. A 271 (1988) 591.
[113] K.J. McCarthy and J. Fryar, Nucl. Instrum. Methods Phys. Res. A 287 (1990) 613.
[114] J.J. Battista and M.J. Bronskill, Phys. Med. Biol. 23 (1978) 1.
[115] R. Guzzardi and M. Mey, Phys. Med. Biol. 26 (1981) 155.
[116] L. Brateman, A.M. Jacobs and L.T. Fitzgerald, Phys. Med. Biol. 29 (1984) 1353.
[117] G. Harding and R. Tischler, Phys. Med. Biol. 31 (1986) 477.
[118] G. Harding and J. Kosanetzky, J. Opt. Soc. Am. A 4 (1987) 933.
[119] G. Harding, J. Kosanetzky and U. Neitzel, Med. Phys. 14 (1987) 515.
[120] R. Cesareo and S. Mascarenhas, Nucl. Instrum. and Methods in Phys. Res. A 27 (1989).
[121] M. Bavdaz, A. Knochel, P. Ketelsen, W. Petersen, N. Gurker, M.H. Salehi and T. Dietrich, Nucl. Instr. Methods Phys. Res. A 266 (1988) 308.
[122] K. Jones, W.M. Kwiatek, B.M. Gordon, A.L. Hanson, J.G. Pounds, M.L. Rivers, S.R. Sutton, A.C. Thompson, J.H. Underwood, R.D. Giauque and Y. Wu, Adv. X-Ray Anal. 31 (1987) 59.
[123] Y. Gohshi et al., Adv. X-Ray Anal. 31 (1988) 495.